5-2023

An Experimental Investigation of the Effect of Narrowband Freestream Noise on Fundamental Transitional Shockwave-Boundary Layer Interaction Mechanisms

Zane Matthew Shoppell
zshoppel@vols.utk.edu

To the Graduate Council:

I am submitting herewith a thesis written by Zane Matthew Shoppell entitled "An Experimental Investigation of the Effect of Narrowband Freestream Noise on Fundamental Transitional Shockwave-Boundary Layer Interaction Mechanisms." I have examined the final electronic copy of this thesis for form and content and recommend that it be accepted in partial fulfillment of the requirements for the degree of Master of Science, with a major in Aerospace Engineering.

John D. Schmisseur, Major Professor

We have read this thesis and recommend its acceptance:

Phillip A. Kreth, Ryan Bond, Farhan Siddiqui

Accepted for the Council:
Dixie L. Thompson

Vice Provost and Dean of the Graduate School

(Original signatures are on file with official student records.)

An Experimental Investigation of the Effect of Narrowband Freestream Noise on Fundamental Transitional Shockwave-Boundary Layer Interaction Mechanisms

A Thesis Presented for the

Master of Science

Degree

The University of Tennessee, Knoxville

Zane Matthew Shoppell

May 2023

This paper is dedicated to my parents, Lori and Gary, for their endless support of all my endeavours.

"Aut inveniam viam aut faciam"

Acknowledgments

I would like to thank my advisor, Dr. John Schmisseur, first and foremost, for providing me with the opportunity to pursue a career in hypersonic aerodynamics. You gave me a chance to grow and develop as an engineer and a person in ways I did not think were possible. I would also like to thank my committee: Dr. Phillip Kreth, Dr. Ryan Bond, and Dr. Farhan Siddiqui. The guidance you all provided throughout this process was invaluable. Additionally, I would like to thank the engineering support staff, especially Mr. John Strike for his guidance and assistance with both designing the models and operating the Mach 2 blowdown facility, Mr. Larry Alexander for his assistance in operating the Mach 2 blowdown facility, and Mr. Kirk Davenport for manufacturing the models used in this experiment. Furthermore, I would like to thank the UTSI machinists – Mr. Gary Payne, Mr. Jack LeGeune, Mr. Jason Riley, and Mr. Dennis Harbin – for their excellent work and willingness to pass their knowledge on to others.

I want to extend my gratitude to my peers in the HORIZON research group and at UTSI for exposing me to new ideas and ideals. In particular, I would like to thank James Chism for pushing me to better myself, Lauren Lester for our lengthy discussions regarding SBLIs and future research areas, and Dr. Theron Price for encouraging me to have confidence in my scientific instincts and methods. I especially want to thank Jacob Butera for all of his help, support, and friendship over the past two years. My experiments would have gone poorly without another set of hands to assist.

Lastly, I would like to thank those who helped me along my journey. First, thank you to my family for supporting me in everything I have pursued; I love all of you deeply. Second, I would like to thank my high school teacher and football coach, Mr. Joseph Morsaw, for encouraging me to pursue a degree in engineering and for all his guidance over the years.

Next, I want to thank Dr. Shawn Keshmiri at the University of Kansas for pushing me to better myself as an aerospace engineer and for recommending me to apply to UTSI for graduate school. Finally, I thank Dr. Ray Taghavi at the University of Kansas for his wonderful mentorship and for taking a chance on me, as without your support, I would have never made it to where I am today.

Abstract

Recent work at the University of Tennessee Space Institute has demonstrated that the resonant behavior observed in the spectra of cylinder- and blunt-fin-generated XSBLIs is connected to fundamental fluid mechanisms within the boundary layer. Therefore, a test campaign was conducted to characterize the fundamental mechanisms that drive the low-frequency unsteadiness in cylinder- and blunt-fin-generated shockwave-boundary layer interactions, specifically shockwave-boundary layer interactions in which the incoming boundary layer is undergoing a laminar-to-turbulent transition. This research aims to develop a deeper understanding of such interactions and characterize the resonant behavior observed in past work by varying the sweepback angle of a hemicylindrical blunt fin in the UTSI Mach 2 Blowdown Facility.

A z-type schlieren setup provided a qualitative understanding of the flowfield. Quantitative results were extracted from the qualitative images using image processing techniques developed within MATLAB. Previously reported freestream narrowband noise in the University of Tennessee Space Institute Mach 2 Blowdown Facility was measured in the spectral content of the leading-edge shockwave and in the boundary layer. The unswept case showed excellent agreement with previously reported results. However, the swept blunt-fins did not exhibit the same narrowband spectral content as the unswept blunt-fin, but instead showed a broadening of the spectral content as the sweep angle was increased. Additionally, the scale of the interactions decreased, as expected, with the reduction in shock strength. Furthermore, the calculated Strouhal numbers for the swept fins showed excellent agreement with prior research.

Table of Contents

List of Tables

List of Figures

Nomenclature

Abbreviation

CCD Charge-Coupled Device

CMOS Complementary Metal Oxide Semiconductor

HORIZON High-speed Original Research and Innovation Zone

NaN Not a Number

PIV Particle Image Velocimetry

SBLI Shockwave-Boundary Layer Interaction

SLBLI Shockwave-Laminar Boundary Layer Interaction

STBLI Shockwave-Turbulent Boundary Layer Interaction

STP Standard Temperature and Pressure

TALon Tennessee Aerothermodynamics Laboratory

UTSI University of Tennessee Space Institute

XSBLI Transitional Shockwave-Boundary Layer Interaction

Greek

α Angle of Attack

δ Boundary Layer Thickness

γ Ratio of Specific Heats

$\hat{\phi}$ Windowed Periodogram

ρ Density of a Fluid Medium

Latin

$\dot{m}$ Mass Flow Rate

d Diameter of Cylinder or Hemicylindrical Blunt-Fin

f Frequency

f_L Focal Length

G_{xx} Estimate of Power Spectral Density (Welch's Method)

h Specific enthalpy

k Gladstone-Dale Coefficient

M Mach Number

m Mass

n Index of Refraction

P Power of Temporal Window

p Pressure

Re Reynolds Number

Re/x Unit Reynolds Number

S Samples

s Visual Thickness of Shockwave

T Temperature

T_c Characteristic Period

U Velocity in the Streamwise Direction

u Boundary Layer Velocity in the Streamwise Direction

x Coordinate in the Streamwise Direction

y Coordinate in the Wall-normal Direction

z Coordinate in the Spanwise Direction

Subscripts

0 Stagnation Condition

∞ Freestream Condition

c Characteristic

e Edge Condition

w Wall Condition

Superscripts

$'$ Fluctuation from Mean Value

Chapter 1

Introduction

1.1 Motivation

In recent years, supersonic and hypersonic aircraft development has become increasingly important to commercial- and defense-oriented aerospace applications. Due to the dynamic operating conditions experienced in the flight regimes of these vehicles, the design of the subsystems for such aircraft require a highly integrated approach. Consequently, understanding the behavior of the aerothermodynamics on the vehicle becomes critical as it provides the boundary conditions for the other subsystems. Therefore, mitigating extreme aerothermodynamic loads is vital for ensuring the aircraft's operational health.

Shockwave-boundary layer interactions (SBLI) are a primary source of risk for high-speed aerospace systems. These interactions create large localized acoustic and thermal loads, which could lead to structural failure [3, 33, 84, 20]. As these interactions are present in external flows (e.g., control surfaces and wing structures) and internal flows (e.g., engine inlets and isolators), understanding these phenomena is essential for vehicle development.

SBLIs are driven by two primary factors: the incoming state of the boundary layer and the geometry of the shockwave generator. The majority of SBLI research in the past has focused primarily on interactions occurring with either a laminar incoming boundary layer (SLBLI) or a turbulent incoming boundary layer (STBLI). However, using experimental and computational methods, laminar interactions can be predicted reasonably well, so relatively little research currently focuses on these phenomena. Despite the

well-characterized nature of SLBLIs, the understanding of the STBLIs still needs to be improved. Characteristically random processes drive the turbulent boundary layer and STBLIs; therefore, such interactions are much harder to predict analytically. The STBLI is characteristically unsteady and chaotic, with high levels of heat transfer occurring on the surface of the aircraft; thus, the chaotic phenomena of STBLIs have been under investigation for decades. Modern computational techniques are increasingly accurate in predicting these phenomena. However, as flowfields become increasingly more complex, it will be necessary to supplement the understanding of the basic mechanisms driving the interaction.

In recent years, investigations into the behavior of a shockwave interacting with a boundary layer undergoing transition from a laminar-to-turbulent state have been of increasing interest. In the past, high-speed aerospace systems operated with predominantly turbulent flows to mitigate the chance of flow separation at the sacrifice of increased heat transfer. However, modern high-speed vehicles are designed with extended laminar flow in mind. Consequently, this leads to transition occurring farther downstream, increasing the likelihood that a shockwave will interact with a transitional boundary layer at the junction of a control surface or tail structure. Although the characteristic laminar and turbulent states bind the scale transitional shockwave-boundary layer interaction (XSBLI), these interactions have unique dynamics not present in the limiting states. Transitional interactions exhibit significant changes in scale when alternating between the laminar and turbulent states of the boundary layer. This significant change in interaction scale and the unsteadiness in the limiting turbulent state causes extremely unsteady behavior within the interaction to occur. As a result, XSBLIs are responsible for higher local heat transfer rates than laminar and turbulent interactions.

The state of the incoming boundary layer and the geometry of the shockwave generator can be reframed to present the two primary mechanisms that drive unsteadiness within the XSBLI: an upstream mechanism (boundary-layer state) and a downstream mechanism (separation scale) [9, 49]. The scale and content of the incoming boundary layer drive the upstream mechanism. The phenomena within the separation region drive the downstream mechanism. The strength of this interaction is determined by whether the interaction is closed or open and from the strength of the inviscid shockwave. A closed interaction is

defined as an interaction with strong recirculation occurring in the separation region, such as the interaction produced by a cylinder mounted orthogonal to the surface where the recirculating fluid material along the centerline is "trapped" or "closed." However, an open interaction, such as one caused by a swept compression ramp, is when the separation region is allowed "open up" and allows the separated flow to "sweep" downstream and does not exhibit strong recirculation.

Recent work at the University of Tennessee Space Institute (UTSI) has investigated the behavior of cylinder- and blunt-fin-generated XSBLIs in a Mach 2 blowdown facility [45, 46, 12]. During this investigation, high-amplitude, narrow-band peaks in the spectra were detected in the dynamics of the separation region. Subsequent studies performed by the reporting research group [48, 47, 10, 14, 15] have validated the presence of this frequency and exhibited that the spectra scale analogously with that of classic laminar boundary layer growth theory $\left(\delta \sim \frac{1}{\sqrt{x}}\right)$ when the incoming scale of the boundary layer was increased, thus, implying that the resonant behavior observed in the spectra is connected to fundamental fluid mechanisms within the boundary layer.

1.2 Research Objectives

This research aims to develop a deeper understanding of the dynamic mechanisms in transitional interactions and further characterize the resonant behavior observed in past work. The strength of the XSBLI will be varied in this work by changing the sweep angle of a hemicylindrical blunt-fin in the UTSI Mach 2 Blowdown Facility. An examination of the spectra from the different sweep angles of the shock generator will allow the determination of whether the resonance observed by Lash et al. [47, 45, 48, 46] and Combs et al. [14, 10, 13, 15, 11] is a function of both the boundary layer scale and the interaction strength. This work looks to address the following goals:

1. To characterize the influence of overall interaction strength on the interaction scale.

   The results of this experiment will indicate how the scale of this interaction changes when the sweep angle is varied. The mean location, standard deviation,

and the probability density function (PDF) will be reported and compared to previous literature.

2. To investigate the influence of overall interaction strength on the dynamics of the interaction.

   The results of this investigation will provide insight into the type of dynamic behavior that should be expected at a variety of sweep angles. In addition, this will be compared to the unswept scenario well-characterized in previous literature.

3. To determine whether the upstream or downstream mechanism of unsteadiness drives the resonant behavior observed in previous work.

   The presence of the resonant frequency in the UTSI Mach 2 Blowdown Facility has persisted when increasing the scale of the incoming boundary layer. However, in this work, the distance from the leading edge of the flat plate is insufficient to support the growth and development of superstructures within the boundary layer. Therefore the unsteadiness should be primarily driven by the downstream mechanism. Thus, if the resonant behavior does not persist with a reduction in the scale of separation, it would indicate that the scaling of the resonant behavior is a function of the downstream mechanism, as the strength of this mechanism decreases with an increase in the sweepback angle of the hemicylindrical blunt-fin.

Chapter 2

Overview

This chapter will summarize pertinent literature and fluid dynamic phenomena relevant to the discussion of results. In this chapter, cylinder and fin will be used interchangeably, as previous research has shown that the phenomenon recorded upstream of the shock generator is nearly identical [47, 21, 7]. First, a summary of the cylinder- and blunt-fin-generated shockwave-boundary layer interaction (SBLI) is discussed, emphasizing the general structure and characteristic length scales. Subsequently, the transitional shockwave-boundary layer interaction (XSBLI) is discussed in further detail. This section emphasizes the general XSBLI flowfield and discusses the mechanisms of unsteadiness present in transitional and turbulent interactions. Finally, the narrowband spectral content observed in the UTSI Mach 2 blowdown tunnel will be discussed.

2.1 Cylinder- and Blunt-Fin-Generated Shockwave-Boundary Layer Interactions

The unswept cylinder-generated SBLI is known as a dimensional interaction [68, 79]. Dimensional interactions are defined as interactions in which the shock generator introduces a secondary length scale, the cylinder diameter in this case, similar in size to the boundary layer thickness [68, 83, 49]. In such a scenario, the SBLI must be scaled to both the boundary layer thickness and the diameter of the cylinder to meet semi-infinite conditions.

Nevertheless, the traditional low-frequency unsteadiness observed in non-dimensional SBLIs still occurs in dimensional interactions. Fig. 2.1a shows the basic flow structure and streamlines of an incompressible separation event to provide an understanding of the baseline flow geometry. An adverse pressure gradient (strengthened by the presence of the inviscid bow shock) is created at the face of the cylinder inducing separation of the incoming boundary layer. The separation of the shear layer causes the formation of a shockwave. This shockwave impinges upon the inviscid bow shockwave thus bifurcating the shockwaves and producing a closure (reattachment) shockwave. The bifurcated region resembles the shape of the Greek letter λ, and therefore, the separation shock foot and closure shock foot are referred to as the λ_1 and λ_2 shocks, respectively. A separation bubble is present along the centerline of the interaction between the λ_1 and λ_2 shocks. Due to the entrapment of fluid material along the centerline of the separation region, this is known as a closed interaction. The dynamics and scaling of this region will be discussed in-detail in later sections. A representation of a shockwave-turbulent boundary layer interaction (STBLI) is shown in Fig. 2.1b below.

To account for the dimensionality of the cylinder-generated interaction, several scaling parameters have been developed to define a semi-infinite interaction. Dolling and Bogdonoff [21] determined that the ratio of the triple point height, h_{tp}, to the cylinder/fin height, h, must be $h/h_{tp} >$ 2-3 to ensure a semi-infinite condition. However, they also suggested the more widely-used height-to-diameter ratio of $h/d > 2.4$. This parameter is favorable as it accounts for the secondary characteristic length scale of the interaction, and does not require knowledge of the triple point height when designing a model. Lindörfer et al. [52] investigated and verified additional scaling factors based on the ratio of the two characteristic length scales d/δ. They showed through numerical schlieren and surface pressure profiles that blunt-fin-generated interactions should be independent of the Mach number and Reynolds number for $d/\delta \gtrsim 2$.

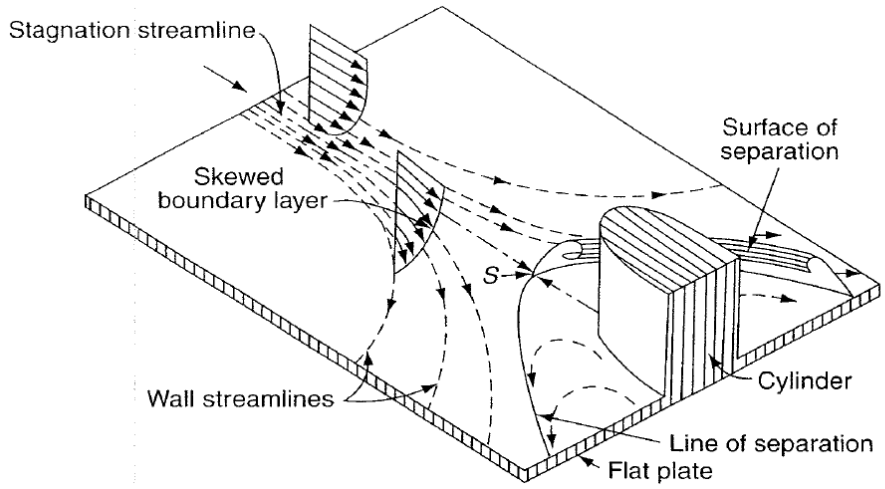

(a) Three-dimensional separation in flat-plate incompressible flow against a cylindrical obstacle. Image taken from White [87] with permission from McGraw Hill LLC.

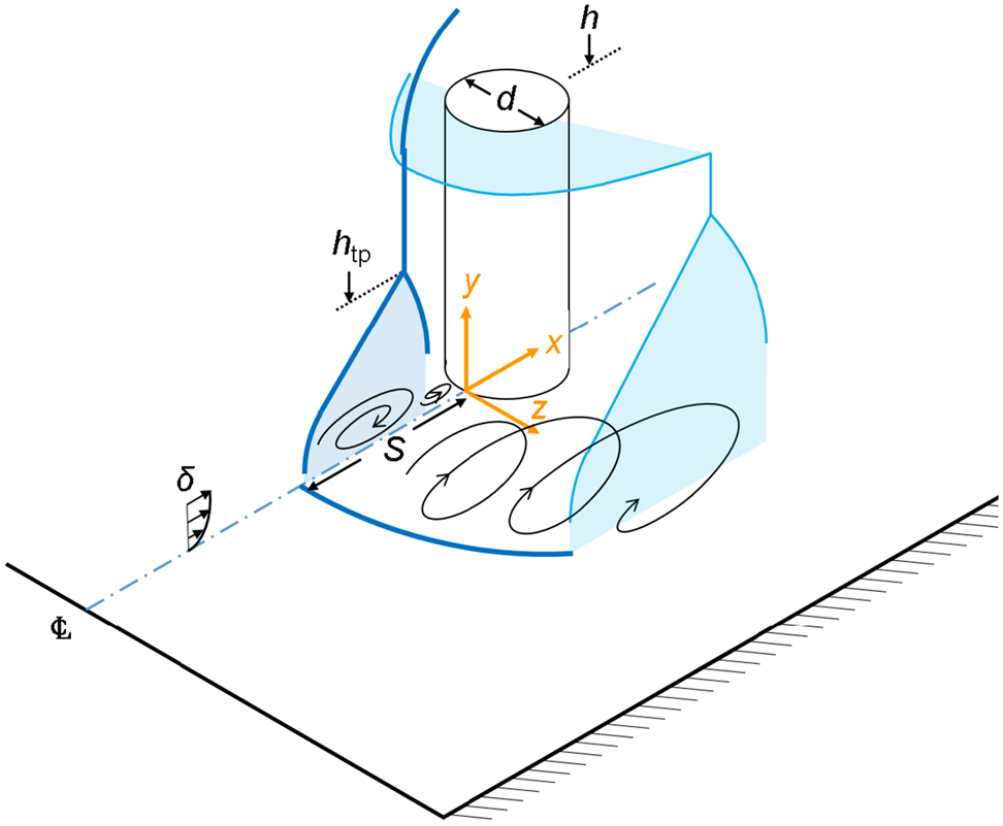

(b) Three-dimensional separation occurring in a flat-plate cylinder-generated SBLI. Image taken from Lindörfer et al. [52] with permission from Springer Nature.

Figure 2.1: Three-dimensional separation flow geometry for (a) an incompressible flow, and (b) a compressible flow w/ a SBLI present.

2.2 Transitional Shockwave-Boundary Layer Interactions

The transitional shockwave-boundary layer interaction is defined as an SBLI that occurs when the boundary layer state is undergoing a laminar-to-turbulent transition. Whereas the definition of STBLIs are rather unambiguous, the XSBLI is much harder to characterize. Threadgill et al. [79] suggest that the characterization of transitional interactions can be easily grouped into two categories, upstream-transitional or interaction-transitional. Upstream-transitional interactions are defined as XSBLIs in which intermittency is measured in the incoming boundary layer, whereas interaction-transitional is defined as a XSBLI in which the incoming boundary layer is intermittency-free and the interaction induces the transitional behavior within the shear layer. For the work in this paper, all interactions are characterized as upstream-transitional as Lash et al. [47] measured intermittency in the incoming boundary layer for similar model geometries.

Standard XSBLI Flowfield

The following paragraph is adapted, with minor changes, from the work of Shoppell et al. [70] with full copyright permissions from the American Institute of Aeronautics and Astronautics. The global flowfield of an unswept blunt-fin-induced XSBLI in the UTSI Mach 2 blowdown tunnel is illustrated in Fig. 2.2. At the leading edge, a shockwave is generated by the sharp edge of the $\alpha = -5.5^{\circ}$ flat plate and the boundary layer develops along the surface. As the boundary layer propagates downstream, it starts to undergo laminar-to-turbulent transition until it reaches the shock interaction region. The shock interaction region possesses a characteristic lambda shape that is composed of the inviscid bow shock and the bifurcated shock below it along with a separation bubble. The separation shock is located upstream of the separation bubble. This shock foot is on average about $2d$-$3d$ away from the face of the blunt-fin, but it moves in an oscillatory manner in transitional and turbulent interactions. The upstream-influence (UI) shockwave travels upstream intermittently during transitional shockwave-boundary layer interactions. The reattachment shock is located slightly upstream of the fin face. At the intersection of the bifurcated shockwave and the inviscid shockwave,

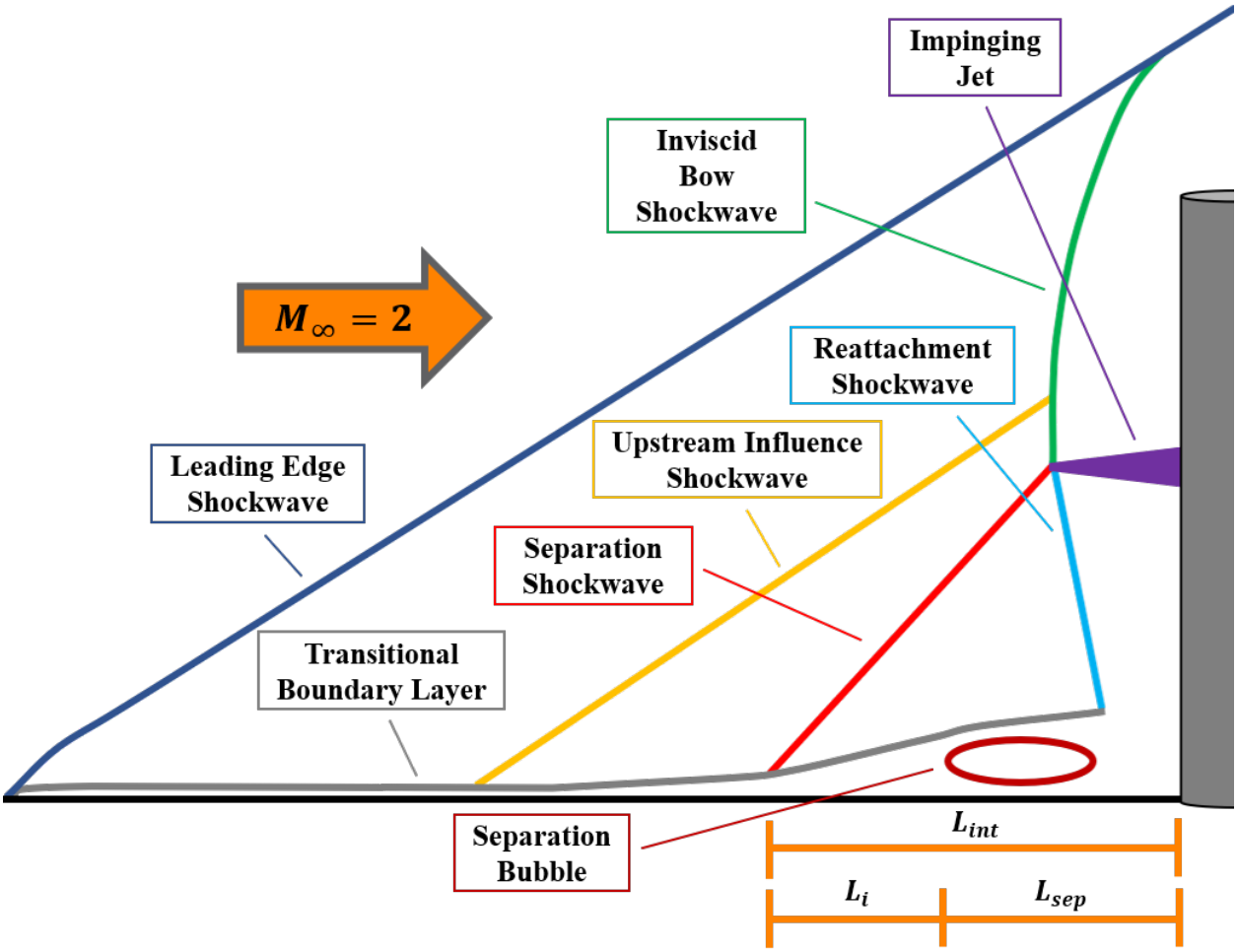

Figure 2.2: The various features of an unswept hemicylindrical blunt-fin-induced transitional shockwave-boundary layer interaction on a flat plate at Mach 2 freestream conditions. Image taken from Shoppell et al. [70] with permission from the American Institute of Aeronautics and Astronautics.

known as the triple-point, a jet which generates vortical structures is formed. This jet moves in the wall-normal direction along the hemicylindrical face of the blunt-fin in tandem with the unsteady movement of the triple point and is responsible for the highest surface heating rates on the fin [47].

2.2.1 Mechanisms of Unsteadiness

The shockwave-boundary layer interaction is driven by two primary mechanisms of unsteadiness: an upstream mechanism, and a downstream mechanism. This unsteadiness is especially dominant in the low-frequency range ($1\ \text{kHz} \leq f \leq 10\ \text{kHz}$) where the SBLI exhibits a characteristic broadband distribution in the spectra. The upstream mechanism is driven by the incoming state of the boundary layer and is driven by the incoming flowfield in addition to the receptivity process. However, the downstream mechanism is driven primarily by unsteadiness within the separation region. The downstream mechanism has been found to be the dominant mechanism for the low-frequency unsteadiness within the interaction especially in strongly separated flows. However, the upstream mechanism can couple with the downstream mechanism in weakly separated flows and behave as a weak forcing function. An in-depth discussion of these mechanisms and the phenomena behind them is presented in the following sections.

Upstream Mechanism

The incoming state of the boundary layer is primarily responsible for the unsteadiness produced upstream of the interaction region. As a result, the unsteadiness within a stable, incoming laminar boundary layer is essentially negligible, whereas an incoming transitional or turbulent boundary layer is highly unsteady in nature. Therefore, it is of critical importance to understand the basic phenomena that drive the unsteadiness within the boundary layer in addition to discussing the impact of the incoming boundary layer on the interaction.

The upstream mechanism of unsteadiness for SBLIs is a function of the incoming boundary layer state, and consequently, the incoming freestream conditions of the tunnel; hence, the process of laminar-to-turbulent transition can rapidly become complex in nature.

However, through experimental and computational research, the basics of this process have been well-defined. A commonly used "road map" describing laminar-to-turbulent transition was developed by Morkovin [55, 56] in the 1960s. This road map, shown in Fig. 2.3, breaks the process down into five potential paths a boundary layer can follow to transition to turbulence. As noted at the top of Fig. 2.3, the path to turbulence is largely defined by the amplitude of the environmental disturbance introduced to the system. The effects of these disturbances are often characterized using linear stability theory to approximate whether the amplitude of the disturbances are significant enough to induce unsteadiness within the flow [87]. The process in which these instabilities manifest into the boundary layer is known as the receptivity process.

The receptivity process is critical to the development of unsteadiness within the boundary layer upstream of the interaction region, however, the receptivity process only characterizes the generation of instability waves and not the spatiotemporal evolution of the waves. The amplitude of the incoming disturbance defines the initial conditions for the frequency and phase of the breakdown process [67, 87]. In supersonic flows with a shockwave present at the leading edge of the test model, three types of waves can force instabilities into the boundary layer: acoustic waves (pressure fluctuations), entropic waves (temperature or density fluctuations), and vortical waves (turbulence) [88, 89, 67, 55, 56, 57]. As expected, the propagation of the acoustic waves occurs at the local acoustic velocity whereas the entropic and vortical waves are convected by the velocity flowfield. An example of these processes is shown in Fig. 2.4 below. The instability waves generated from the aforementioned waves can transition towards turbulence via several different mechanisms. Understanding these mechanisms will be important for later sections.

Using the simplified road map in Fig. 2.3, it can be seen that five standard paths to transition are defined. It should be noted that the road map is a very simplified representation of a very complex, multivariable problem, but to represent the process in a straightforward manner, simplifications to the process were made to provide a standard approach to boundary layer transition. Saric et al. [67] describe these five paths as the following:

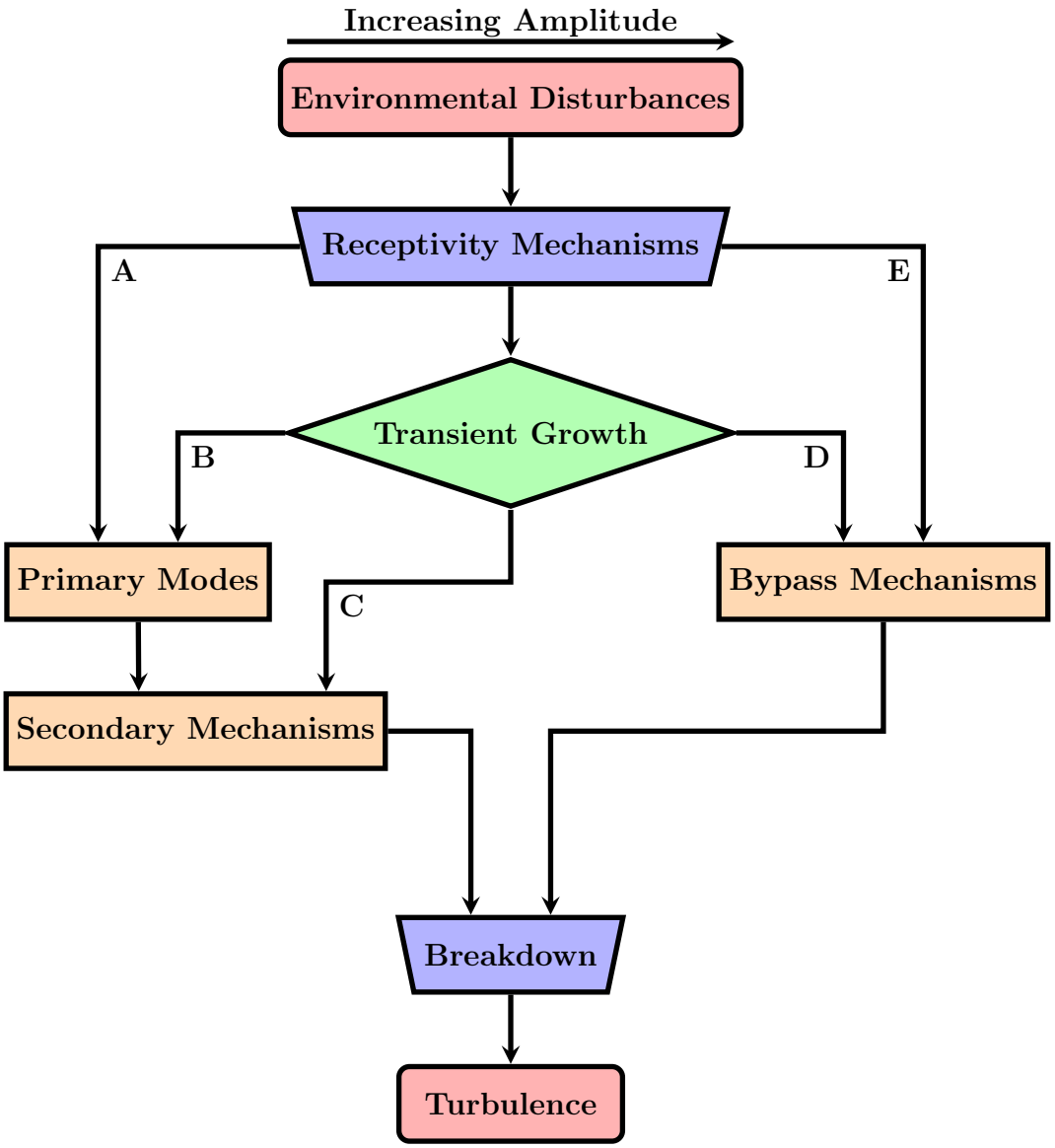

Figure 2.3: The road map of laminar-to-turbulent boundary layer transition as defined by Morkovin [55, 56, 57].

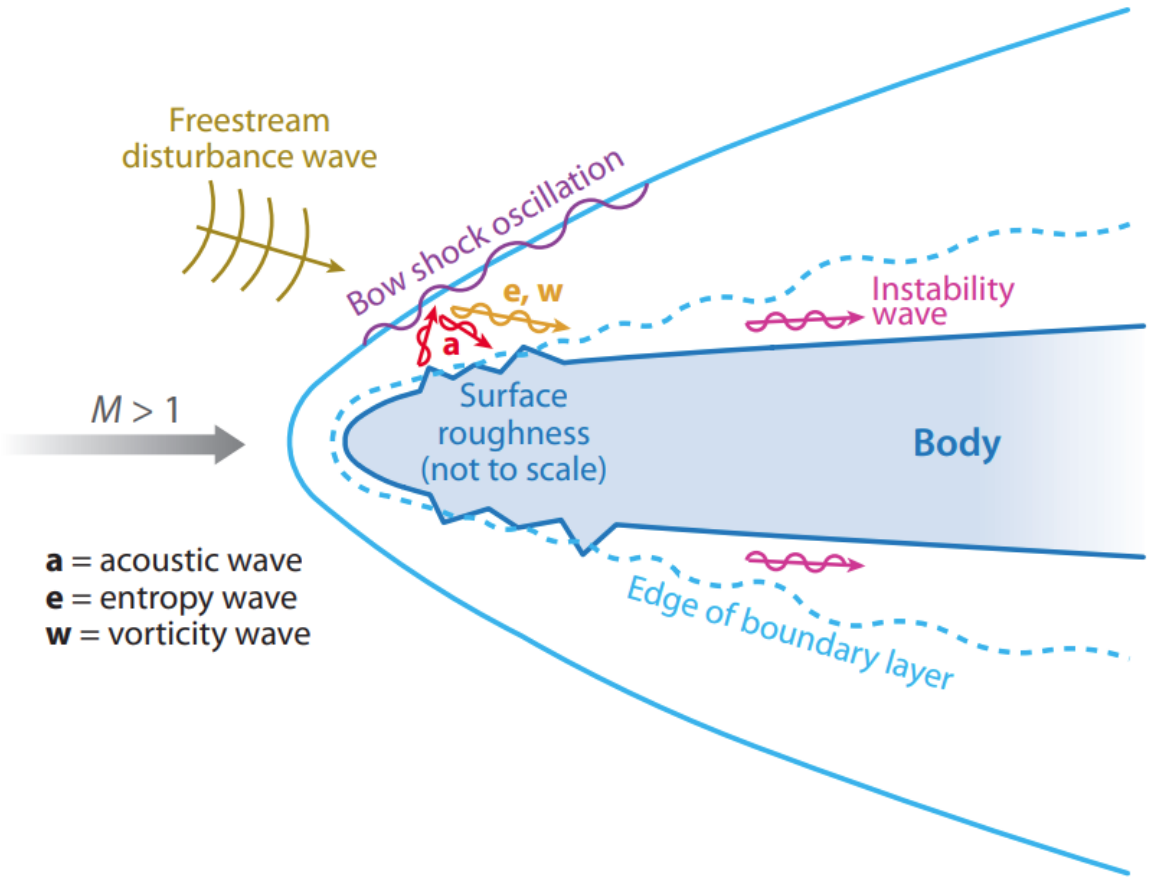

Figure 2.4: A schematic of the receptivity process in a high-speed compressible flow induced by free-stream disturbances and surface roughness. Figure taken from Zhong and Wang [89] with permission of Annual Reviews.

A. The linear stability breaks down and the primary modes, known as the Mack modes for the compressible regime (see Mack [53, 54]), induce transition into turbulence.

B. The transient growth causes spanwise inflections to develop within the primary instability modes.

C. The transient growth distorts the boundary layer base state and causes the secondary mechanisms (i.e., Görtler, crossflow) to dominate the transition to turbulence.

D. The transient growth of the instabilities causes the boundary layer to directly transition to turbulence.

E. The amplitude of freestream disturbances are potent enough to cause a direct bypass to turbulence to occur.

While receptivity provides an avenue for narrowband noise to persist, the structures and superstructures that form during laminar-to-turbulent transition process also have a significant impact on the interaction. Erengil and Dolling [26] proposed that the incoming boundary layer is responsible for the high-frequency jitter of the separation shock foot. Beresh et al. [4] detected a strong correlation between the instantaneous momentum fluctuations within the boundary layer to the movement of the separated shock foot. They suggested that when the boundary layer quickly develops a fuller profile, the downstream shock motion occurs. Hou et al. [35] observed similar phenomena in the boundary layer and measured that during downstream motion (e.g. bubble-collapse) the boundary layer profile was $\sim 0.04U_\infty$ fuller than when the separation shock was travelling upstream. Ganapathisubramani et al. [27] later, using particle image velocimetry (PIV), measured large turbulent superstructures, approximately $\mathcal{O}(40\delta_0)$ in length, in the logarithmic region of the incoming boundary layer. Humble et al. [37, 36, 39, 38] conducted further PIV studies to observe the effect of the superstructures, and found that superstructures are responsible for the spanwise "wrinkling" of the separated flow, and that the superstructures are not responsible for the movement of the separation shock. It is clear that the upstream mechanism has an effect on the unsteadiness of the separation region, however, it is not responsible for the low-frequency, large-scale movement of the separation shockwave.

Downstream Mechanism

The other dominant source of low-frequency unsteadiness in SBLIs is the downstream mechanism. Recent consensus [60, 82, 9] has described the downstream mechanism as a product of the global instability within the separation region (see Souverein et al. [71, 72] and Clemens and Narayanaswamy [8, 9]). Piponniau et al. [60] proposed the unsteadiness within the separation region was due to the entrainment of the separation region from the separating shear layer. Eq. 2.1 describes the characteristic timescale, T_c, that is driven by the ratio of mass recirculated upstream (or reverse), $m_{reverse}$, to the mass entrainment rate from the shear layer, $\dot{m}_{entrain}$, as described by Piponniau et al. [60]. Eq. 2.2 indicates that inverting the characteristic timescale yields the characteristic oscillation frequency of the separation bubble, f_c.

$$T_c = \frac{m_{reverse}}{\dot{m}_{entrain}} \tag{2.1}$$

yielding a characteristic oscillation frequency of:

$$f_c = \frac{1}{T_c} \tag{2.2}$$

Dupont et al. [24] further investigated the entrainment-discharge due to the formation of a shear layer as the primary source of unsteadiness within the separation region. They found that the separated shear layer did indeed share similar properties to compressible, canonical mixing layers. The mixing and spreading rate of the shear layer as a method of entrainment into the separation bubble were boosted by the recirculation of the flow; however, compressibility effects hampered the development of vertical velocity fluctuations as hypothesized by Brown and Roshko [6].

Another theory as to the source of the low-frequency behavior of the interaction was suggested by Pirozzoli and Grasso [61]. Pirozzoli and Grasso suggested that the low-frequency shock motions could be a result of acoustic resonance induced by the interaction of a shockwave with a vortical structure. In their model, the interaction of the separating shear layer and the separation bubble behaves analogously to an acoustic amplifier that highlights coherent "tones" in the flow. These tones propagate back upstream through the subsonic

region present beneath the separation bubble and create a feedback loop with the shear layer amplification process. Pirozzoli and Grasso [61] relate this process to the Rossiter modes that occur in cavity flows, thus providing a non-linear mechanism for amplitude modulation in the interaction.

The presence of reverse subsonic flow within the interaction region has been known for decades, however, in the work of Tester et al. [75] the region propagates further upstream than previously thought. As shown in Fig. 2.5, the region of upstream flow is present in both transitional (Fig. 2.5a), and turbulent interactions (Fig. 2.5b). Although upstream velocity should be expected within a recirculation event, the thin subsonic region that persists farther upstream indicates a larger streamwise region of subsonic flow than expected. This region permits the propagation of information back upstream within the boundary layer, thus allowing for the downstream mechanism to propagate fluid properties upstream of the separation region. The lack of the downstream velocity "bubble" present in Fig. 2.5b for the transitional case (Fig. 2.5a) indicates that fluid properties (mass, momentum, and energy) in transitional interactions have a much greater likelihood to persist upstream.

Lash et al. [47] correlated the thickening of the upstream boundary layer to the movement of the separation shock foot and saw excellent agreement between the spectral content of both features. As the transitional cases showed the strongest agreement, this is likely due to a mechanism propagating through the subsonic region computed by Tester et al. [75]. As the strength of the separation region is dependent on the magnitude of the adverse pressure gradient [41, 87], the growing separation length could be directly tied to the propagation of higher pressures upstream into the boundary layer before an eventual collapse of the separation bubble once the adverse pressure gradient weakens. Priebe and Martin [65] observed an increase in wall pressure equal to $\frac{\Delta P_w}{P_\infty} \approx 0.3$ during the bubble-collapse event. In addition, a velocity fluctuation of $\frac{u'}{U_\infty} \approx 0.03$ was observed in the lower boundary layer. Similar velocities have been measured during previous bubble-collapse events and downstream sweeps of the separation shock foot by Beresh et al. ($\frac{u'}{U_\infty} \approx 0.025$) [4], Hou et al. ($\frac{u'}{U_\infty} \approx 0.04$), and Gonsalez and Dolling ($\frac{u'}{U_\infty} \approx 0.03$) [30]. However, it should be noted that these velocity fluctuations are not a dominant mechanism in the interaction as Priebe and Martin [65] found the coherence between the momentum transfer rate fluctuations and the

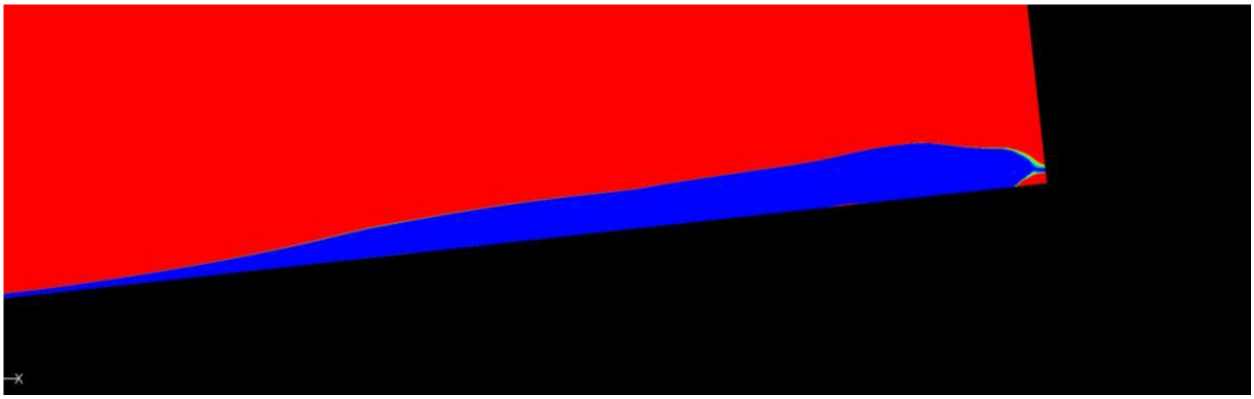

(a) The XSBLI recirculation region.

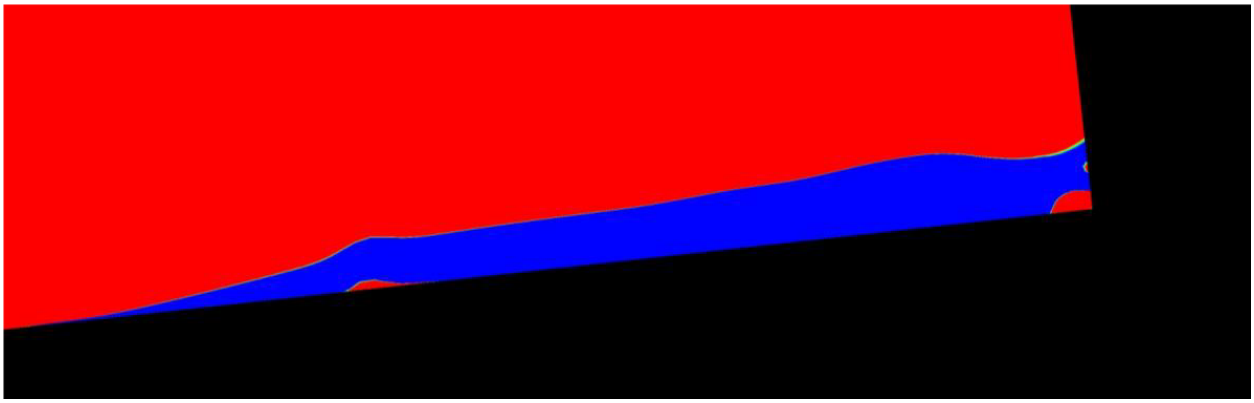

(b) The STBLI recirculation region.

Figure 2.5: Streamwise velocity contours of the centerline upstream of a cylindrical shock generator. Note that flow moves from left-to-right. The red indicates downstream flow whereas blue indicates upstream flow. This figure was taken from Tester et al. [75] with permission from the American Institute of Aeronautics and Astronautics.

separation shock motion to be only about 0.25. Even so, strong separation events, such as a unswept blunt-fin-induced separation, are extremely sensitive to upstream perturbations [9, 82].

Clemens and Narayanaswamy [9] offer a simple approach to predicting this required pressure change needed to induce the collapse of the separation bubble by using the ratio of turbulent fluctuations, u', in the momentum transfer rate, $\dot{m}u'$, defined in Eq. 2.3 and Eq. 2.4, to the change in pressure force (Eq. 2.5). Clemens and Narayanaswamy show that when the ratio of these factors approach unity, the collapse of the separation region occurs. The increase in pressure causes the separation bubble to grow in length which triggers the mechanism presented by Dupont et al. [24] where the mass-entrainment to the separation region from the separated shear layer is overwhelmed by the recirculation of mass upstream. This is especially strong in the case of blunt-fin-induced SBLIs as the recirculation is due to both the reattachment shockwave in addition to the geometry of the shock generator.

$$\dot{m}u' = \bar{\rho}\bar{u}Au' \tag{2.3}$$

rearrange using freestream conditions for average values:

$$\dot{m}u' = \frac{P_\infty}{RT_\infty}U_\infty Au' = \gamma P_\infty M_\infty^2 A\frac{u'}{U_\infty} \tag{2.4}$$

dividing by the change in pressure force $\Delta P_w A$ yields:

$$\frac{\text{momentum transfer rate fluctuation}}{\text{change in pressure force}} = \frac{\gamma P_\infty M_\infty^2 A\frac{u'}{U_\infty}}{\Delta P_w A} = \gamma M_\infty^2 \frac{P_\infty}{\Delta P_w}\frac{u'}{U_\infty} \tag{2.5}$$

The velocity fluctuation required for separation bubble collapse was assumed to be $\frac{u'}{U_\infty} = 0.03$ to match the previously discussed empirical velocity fluctuations [30, 4, 35, 65]. The post-shockwave edge conditions were used as the freestream conditions, $M_\infty \to M_e = 1.77$, as the prediction does not account for leading-edge shockwaves. It was found that the pressure change required to approach unity at these conditions is $\frac{\Delta P_w}{P_\infty} \approx 0.13$. From inspection of the centerline pressure data in Fig. 2.6, it can be observed that a $\frac{\Delta P_w}{P_\infty} \approx 0.13$ occurs roughly $3.5 - 4.5$ diameters from the face of the cylinder thus aligning extremely well

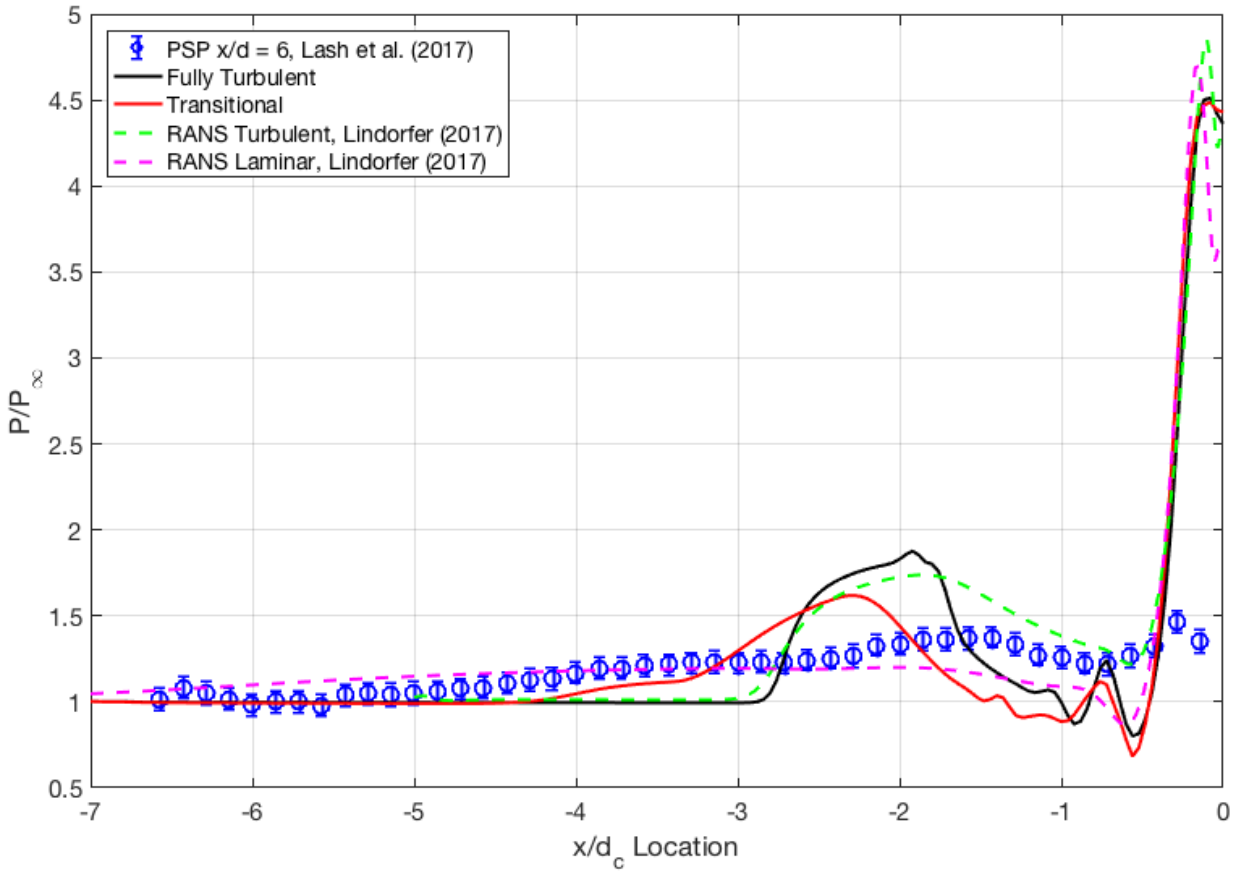

Figure 2.6: Centerline pressure distributions for cylinder-induced shockwave-boundary layer interactions on a flat plate at Mach 2 freestream conditons. Image taken from Tester et al. [75] with permission from the American Institute of Aeronautics and Astronautics.

with the locations measured by Lash et al. [47] and computed by Tester et al. [75] and Lindörfer et al. [51, 50] where the bubble-collapse event manifests.

Touber and Sandham [82] developed a low-order model of the low-frequency motion present within SBLIs using the Reynolds-averaged Navier-Stokes (RANS) equations [66, 58, 74]. In this model, it was found that the SBLI behaved analogously to a low-pass filter as the SBLI caused the **damping of high-frequencies** and the **amplification of low-frequencies** [82, 9]. The model was tested with both white noise (equal amplitudes at all frequencies) and with forced high-pass inputs. They observed great agreement in the PSD data between experimental data and the white noise input. When the model was limited to prevent the presence of the incoming superstructures, approximately $\mathcal{O}(40\delta_0)$ in length, measured by Ganapathisubramani et al. [27, 28, 29], it was shown that the low-frequency shock motion persisted. This indicates that although the incoming boundary layer can have an effect on the shock motion, it is not the dominant mechanism. Additionally, Touber and Sandham [82] observed that the unsteadiness had a characteristic frequency just as Piponniau et al. [60] had observed in his method. Touber and Sandham suggest that the low-frequency motion could potentially be controlled or modified by modifying the natural frequency of the system through wall-boundary conditions. However, they warn that inputs on the order of $10\delta_0/\bar{u}_1$ **could excite the natural frequency** of the coupled shockwave-boundary layer system.

Considering the overall interaction as a dynamic system, many of the previously discussed concepts can be considered as the building blocks within the system. The collapse of the separation region can be thought of as an impulse applied to the system. The rise in pressure due to the bubble-collapse causes a departure from unity in Eq. 2.5 and promotes the mass-entrainment process discussed by Piponniau et al. [60]. Additionally, the subsonic region computed by Tester et al. [75] that is present in three-dimensional closed separation enables the likelihood of the feedback mechanism suggested by Pirozzoli and Grasso [61] occurring. The coupling of the turbulent fluctuations within the boundary layer and the increasing sweepback of the separation shockwave acts as the damper of the system. When the incoming turbulent momentum overcomes the pressure of the separation bubble, the bubble collapses and the cyclical process continues.

2.3 UTSI Mach 2 Freestream Resonance

During an experimental investigation of a cylinder-generated XSBLI in the UTSI Mach 2 blowdown tunnel, the presence of large-amplitude, narrowband spectra were detected in the movement of the separation shock foot by Lash et al. [45]. It was observed that these narrowband spectra scaled analogously with that of classic laminar boundary layer growth theory $\left(\delta \sim \frac{1}{\sqrt{x}}\right)$ when the location of the cylindrical shock generator was moved downstream. Additional research was conducted at the University of Tennessee Space Institute by Lash et al. [48, 47] and Combs et al. [10, 13, 11, 14, 15] to investigate the behavior of the narrowband frequency content at different conditions. Lash et al. [47] showed that the frequency content was not produced by vortex shedding occurring behind the cylindrical shockwave generator by using unswept blunt-fins as a shock generator, and observed very good agreement in the spectral content of the blunt-fin to the cylinder. Combs et al. [11] conducted experiments at additional cylinder locations and reported the same trend as Lash et al. had reported. As the frequency content has been observed with schlieren, pressure sensitive paint (PSP), kulite pressure sensors, and focused laser differential interferometry (FLDI), the narrowband spectra is not due to resonance of experimental equipment. The presence of this frequency is clearly a fluid phenomenon, but the source of it is still unknown.

Pohlman and Chism [unpublished] investigated the tunnel for potential frequency sources using a FLDI system, and observed the presence of narrowband content centered around $\sim$ 3 kHz (see Fig. 2.7) present when probing near the tunnel floor boundary layer. This was the first time that the narrowband spectra had been observed without a model installed in the tunnel and suggested that this phenomenon was more than just a characteristic of a XSBLI. Davenport and Gragston [18] recently observed the same narrowband spectra when performing convective velocity measurements using linear-array focused differential interferometry (LA-FLDI) in the floor boundary layer. The frequency peaks within the narrowband spectra were plotted as a function of streamwise location in Fig. 2.8. A power trend of the form $y = ax^b$ was fit to the frequency peaks with b restricted to a value of -0.5 to maintain the boundary layer scaling. It was found that $f = \frac{12.76}{\sqrt{x/d}}$ had an excellent agreement with the experimental data as the curve fit had an $R^2 = 0.98$. Additionally, the narrowband

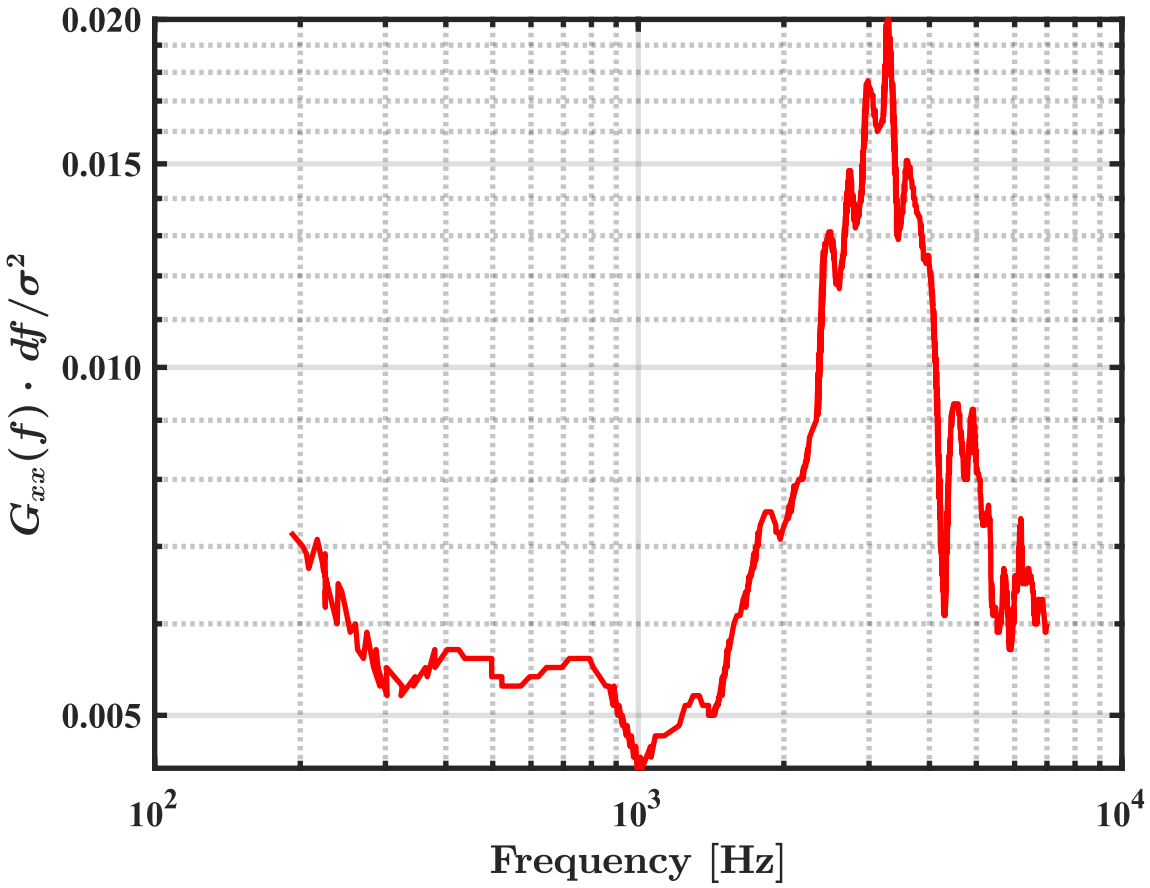

Figure 2.7: A normalized PSD of a FLDI measurement of the freestream near the boundary layer in the UTSI Mach 2 tunnel. This data is unpublished work from Pohlman and Chism of the HORIZON Research Group and was used with their permission. NOTE: The spectra features some aberrations as the original data was extracted from a figure using WebPlotDigitizer and then replotted in MATLAB.

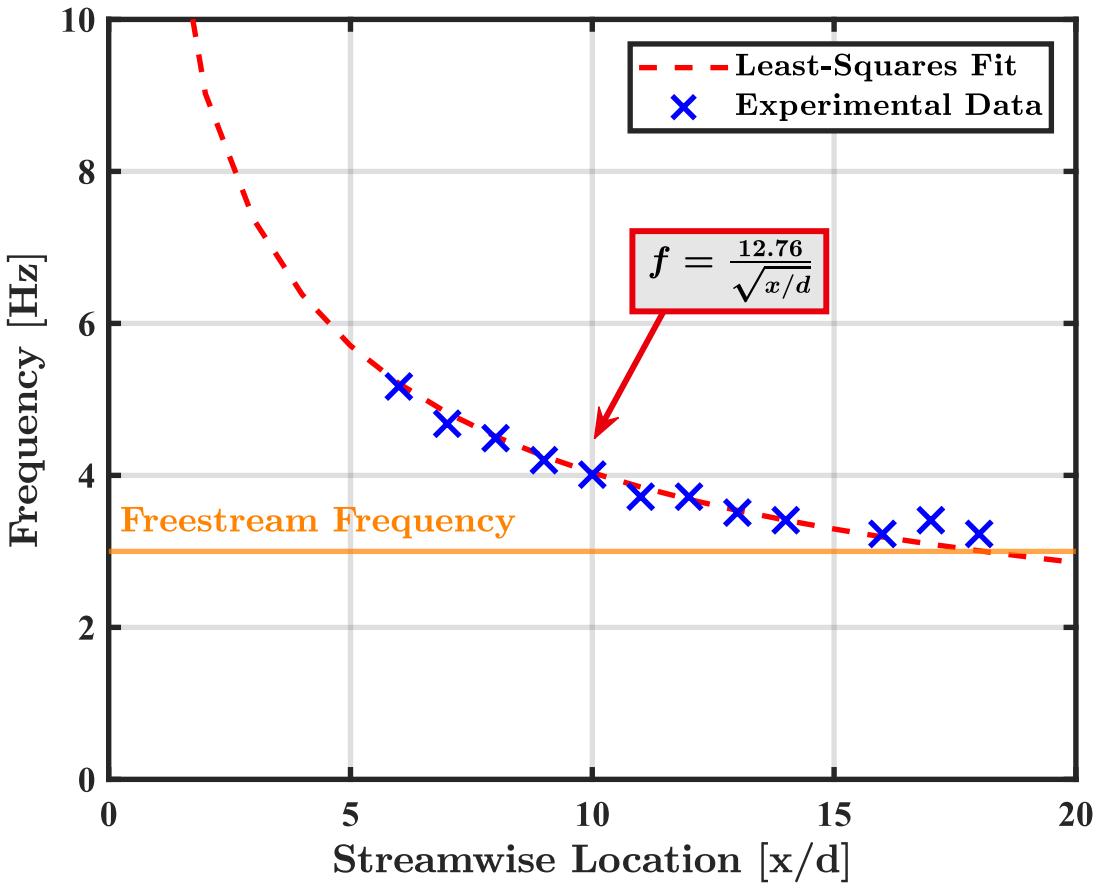

Figure 2.8: A comparison of the resonant peaks observed by Lash et al. [47, 45, 48, 46] and Combs et al. [14, 10, 13, 15, 11] with the streamwise location of the blunt-fin. The data scales well with $\frac{1}{\sqrt{x}}$, indicating the resonant behavior scales analogously to laminar boundary layer growth. A feature of interest is the asymptotic trend of the narrowband spectra towards the frequency content in Fig. 2.7.

spectra appear to approach the freestream frequency asymptotically. This could indicate a possible resonance within the interaction region similar to the mechanism suggested by Pirozzoli and Grasso [61] or the amplification of low-frequencies discussed by Touber and Sandham [82]. Locating the source of this frequency has been proven to be complicated; however, knowing that the frequency content scales aerodynamically, further investigations of the fundamental mechanisms driving XSBLIs can be conducted. This work does not look to provide a source of the narrowband freestream noise but rather to exploit the sensitivity of the interaction to this freestream noise to understand the role of shock strength in 3D canonical interactions.

White et al. [86] showed that a pulsed frequency persists into the boundary layer at the leading-edge of a flat plate through the receptivity process. Although this research was conducted at extremely low freestream velocities of 12 and 15 m/s, the receptivity process has been shown to be very similar between incompressible and compressible flows. Coupling the baseline receptivity process with a leading edge shockwave dramatically increases the likelihood of introducing small disturbances to the boundary layer [89, 88]. Assuming a disturbance wave is introduced at $\sim$ 3 kHz, there is a potential that the leading-edge shockwave will begin to oscillate at approximately the same rate. The oscillation of the shockwave will inherently introduce pressure fluctuations at the same rate as the oscillation, but it could introduce less obvious fluctuations as well. Using Crocco's theorem [17], shown in Eq. 2.6, we can establish a relationship that provides another mechanism for additional fluctuations to manifest into the boundary layer. Crocco's theorem relates the change in stagnation specific enthalpy, ∇h_0, the acceleration, $\frac{\partial \vec{\mathrm{v}}}{\partial t}$, the cross-product of the velocity, $\vec{\mathrm{v}}$, with the vorticity, $\nabla \times \vec{\mathrm{v}}$, to the product of the temperature, T, and the change in specific entropy, ∇s. Introducing curvature to the shockwave through freestream fluctuations creates small amounts of local curvature that induce vortical waves into the post-shockwave flowfield. This approximation is a possible pathway for narrowband noise to manifest in the boundary layer. Furthermore, the spectral content of the leading-edge shockwave and the boundary layer will be analyzed in this work to verify the plausibility of this estimation.

$$T\nabla s = \nabla h_0 + \frac{\partial \vec{\mathrm{v}}}{\partial t} - \vec{\mathrm{v}} \times (\nabla \times \vec{\mathrm{v}}) \tag{2.6}$$

Chapter 3

Methodology

3.1 Experimental Methodology

3.1.1 Experimental Facility and Models

The work in this experiment was conducted in the nominally Mach 2 blowdown wind tunnel at UTSI. The wind tunnel, shown in Fig. 3.1, is connected to a system of high-pressure lines that allow for the facility to be run at a stagnation pressure of 35 psia (241 kPa) for up to two minutes. The Mach 2 facility is unheated and was operated at ambient temperatures of approximately $58.7 \pm 1.8\,^{\circ}\mathrm{F}$ (288 ± 1 K). In this experimental campaign, the tunnel was operated at a freestream unit Reynolds number of $31.2 \pm 0.2 \times 10^{6}\,\mathrm{m}^{-1}$. A summary of the relevant parameters for the UTSI Mach 2 blowdown wind tunnel are shown in Table 3.1.

Figure 3.2 shows a rendering of the hemicylindrical blunt-fin in unswept and swept configurations. The fin has a leading edge diameter $d = 0.125$", and a height $h = 0.5$" in order to satisfy the semi-infinite condition of $h \geq 2.4d$ defined by Dolling and Bogdonoff [21], in addition to satisfying the scaling mechanisms defined by Lindörfer et al. [52]. The blunt-fin was constructed with 3D-printed resin for sweep angles of $\Lambda = 0°$, 10°, 20°, and 30°. All models in this experiment were installed on the flat plate at a streamwise location of $x/d = 6$ to correspond with the most prominent peak reported by Lash et al. [47]. The flat plate, shown in Fig 3.3, is attached to a -5.5° angle mount. The angle mount is connected to a wedge-shaped strut that is attached to the floor plate of the tunnel.

Table 3.1: A summary of freestream tunnel parameters for the 8" x 8" UTSI Mach 2 blowdown facility for this experimental campaign. All static values were calculated using the isentropic relationships. The dynamic viscosity was calculated using Sutherland's law.

Tunnel Parameter	Condition
Mach Number	2
Stagnation Temperature $[K]$	288
Static Temperature $[K]$	160
Stagnation Pressure $[kPa]$	241
Static Pressure $[kPa]$	30.8
Dynamic Viscosity $[\times 10^{-5}\, Pa \cdot s]$	1.09
Re/x $[\times 10^{6}\, \mathrm{m}^{-1}]$	31.2
Maximum Run Time $[s]$	120

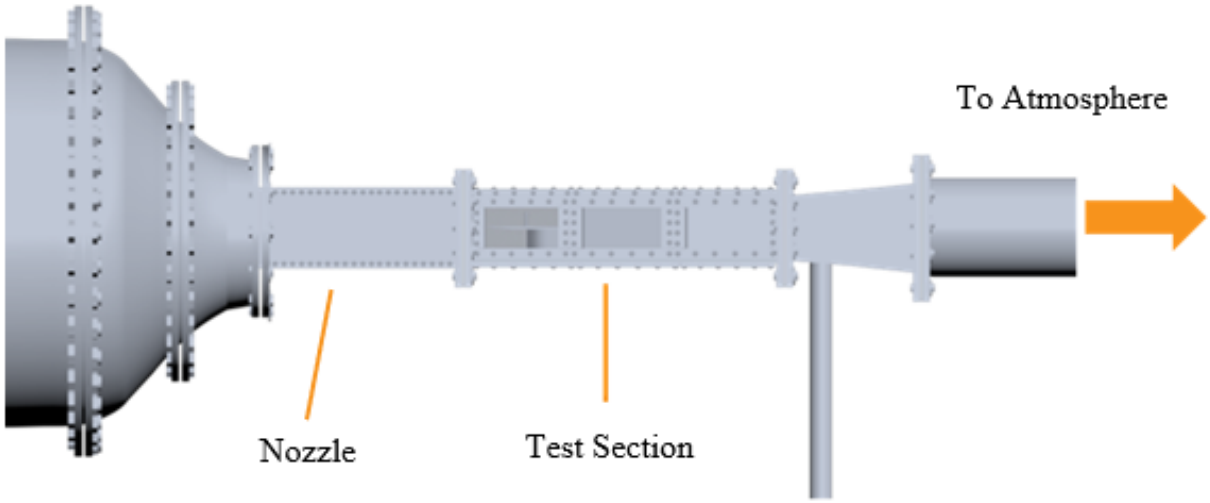

Figure 3.1: A rendering of the UTSI Mach 2 Blowdown Wind Tunnel Facility. Image taken from Shoppell et al. [70]

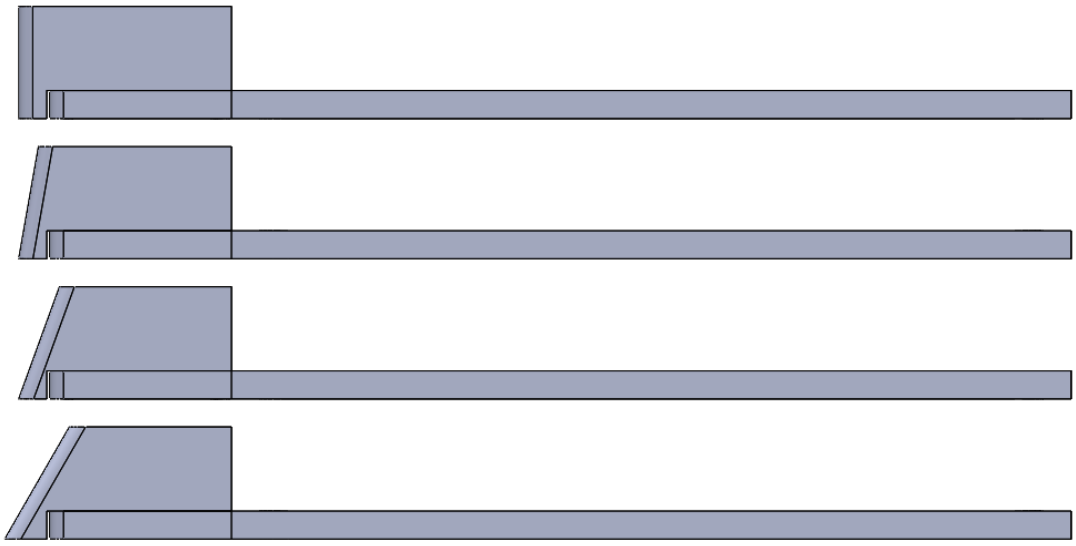

Figure 3.2: A rendering of all blunt-fins used in this work. From top-to-bottom: $\Lambda = 0°$, $\Lambda = 10°$, $\Lambda = 20°$, $\Lambda = 30°$

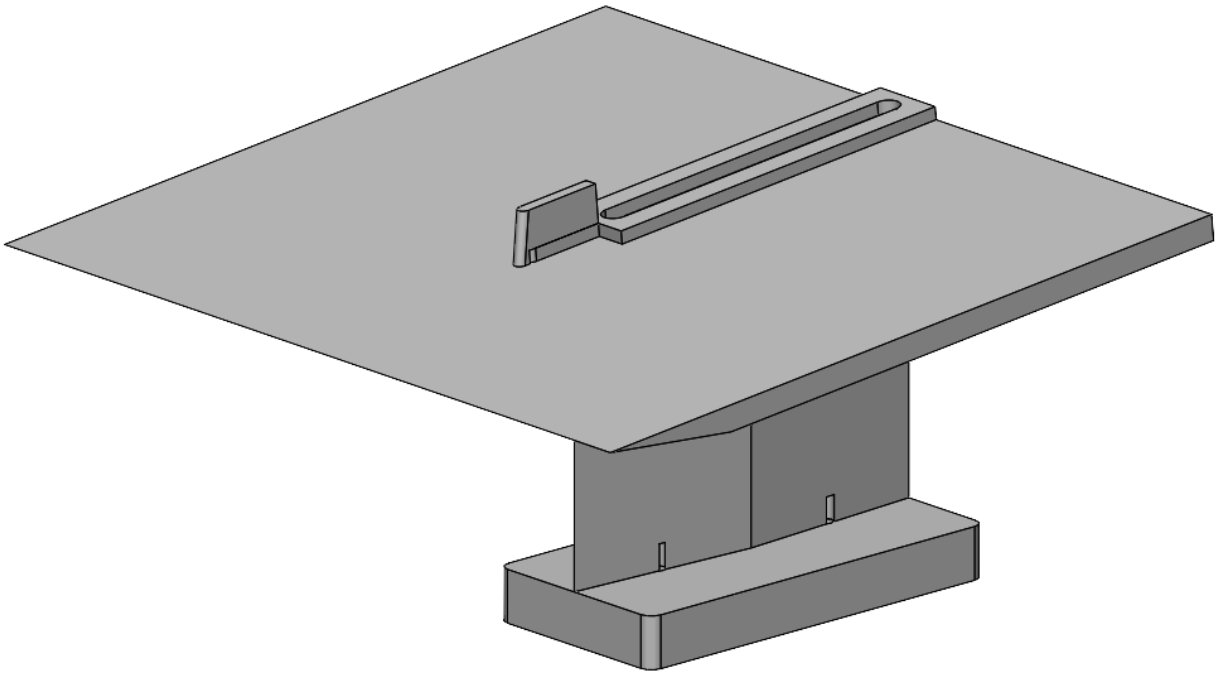

Figure 3.3: A rendering of the $\Lambda = 10^{\circ}$ blunt-fin installed on the flat plate. Image taken from Shoppell et al. [70]

3.1.2 Schlieren

Schlieren is a flow visualization technique with scientific roots recorded as early as the mid-late 17th century by Robert Hooke. During an experiment, Hooke noticed light "streaks", now referred to as *schliere*, that changed with variations in the air density [69, 34]. Subsequently, August Toepler pioneered a schlieren method in the 1800s that is still used as the foundation for most modern setups [80, 81]. Since the invention of the schlieren technique, it has been used predominantly to capture a quasi-average image; however, with the rapid development of high-speed cameras in the past couple of decades, the temporal behavior of flowfields can be captured.

The Gladstone-Dale relation, shown in Eq. 3.1, is the foundation of many flow visualization techniques including schlieren.

$$n - 1 = k\rho \tag{3.1}$$

The Gladstone-Dale relation provides a method to compare the refractivity, $n-1$, to the product of the Gladstone-Dale coefficient, k, and the density of a given fluid medium, ρ. The variable n is known as the index of refraction, and is defined as the ratio of the speed of light in vacuum conditions to the speed of light within a fluid medium. It should be noted that for STP air, $n = 1.00029$ so the refractivity of STP air is relatively low compared to other fluid mediums like water where $n_{20^{\circ}C} = 1.33$. From a basic inspection of the Gladstone-Dale relationship, it can be observed that $\Delta n \propto \Delta\rho$. When the effects of compressibility are no longer negligible ($M \gtrsim 0.3$), density can no longer to be assumed to be a constant value [1, 2, 40]. In this scenario, the changes in the density and index of refraction should now be considered as local variables instead of a global constant for accuracy. Luckily a greater spatiotemporal resolution enabled by digital camera sensors, such as a CCD or CMOS, allows each pixel of the image to be treated analogously to an individual sensor [14, 64]. This allows the local density changes within a compressible flowfield to be resolved on a much higher resolution than previously possible.

Schlieren setups where the event of interest occurs in a field of collimated light are highly recommended as the use of parallel light mitigates the optical aberrations that potentially

occur within a given setup [69]. The presence of a density gradient within this region causes the the deflection of incident light to occur orthogonally to the direction of the collimated light (i.e. if light is along the z-axis then disturbances occur in the x- and y-directions). Essentially these disturbances can be thought of as the divergence, $\nabla \cdot n$, of the collimated light. When the collimated light is focused down to a focal point, the divergence of the incident light rays can be observed if a sharp cutoff, often a knife-edge, is introduced to the system. Consequently, the use of a cutoff allows only a single component of the divergence to be observed. The introduction of a horizontal cutoff allows the observation of $\frac{\partial n}{\partial y}$, whereas a vertical cutoff shows $\frac{\partial n}{\partial x}$. Due to the nature of the boundary layer of interest, a horizontal knife-edge was used in this experiment. Eq. 3.2 shows the relationship between the partial derivative of the refractive index and local density with respect to the y-direction.

$$\frac{\partial n}{\partial y} \sim \frac{\partial \rho}{\partial y} \tag{3.2}$$

A modified z-type schlieren setup, shown in Fig. 3.4, was used in this work. A single optical table was used to mount two optical rails. Two parabolic mirrors were mounted opposite of each other in order to collimate the light rays. In addition, a folding mirror was introduced to the system to provide a more extensive range of spatial access for the camera. In further discussions, the light source and camera sides will be referred to as the "pitch" and "catch" sides, respectively. A summary of the optical components used in this experiment is shown in Table 3.2.

Pitch Side

An in-house light-emitting diode (LED) was operated at a repetition rate of 100 kHz to match the acquisition rate of the camera. The unstructured light generated from the LED was focused using a 2"-diameter condensing lens with a focal length (denoted as f_L to differentiate from frequency) of $f_L = 150$ mm. An iris was placed at the focal point of the converging light field to create a quasi-point light source. The iris was placed 96.75 in (2457.45 mm), or f_L, from the first parabolic mirror. This causes light collimation to occur, and the light is passed from the pitch side to the catch side.

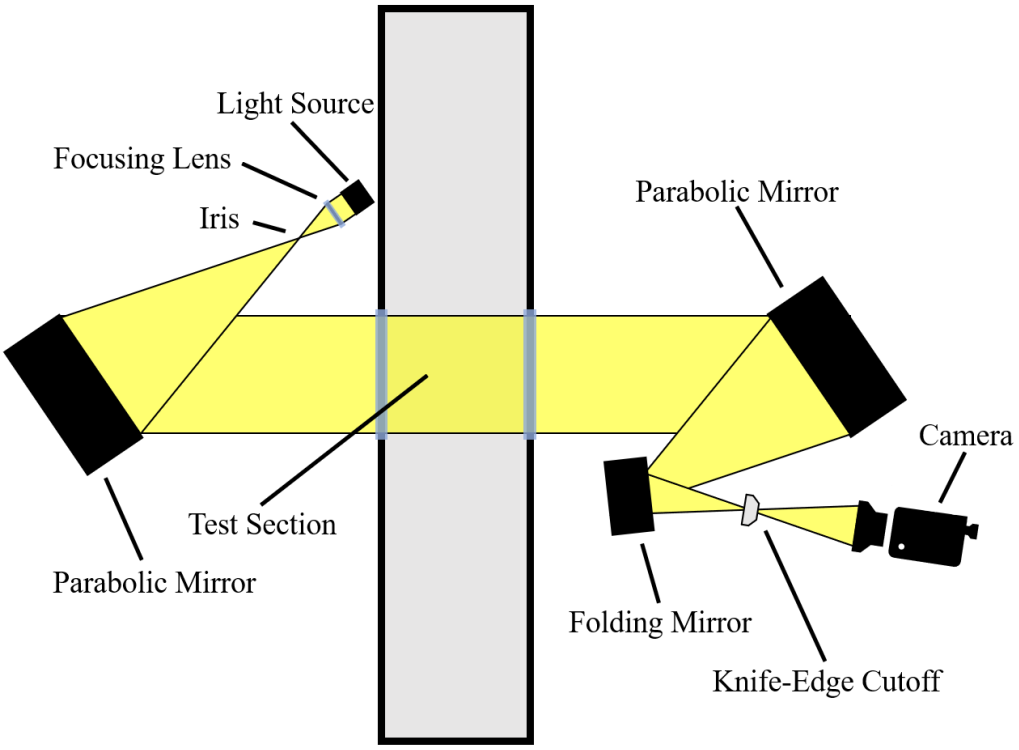

Figure 3.4: A modified z-type schlieren setup modified with the use of a folding (flat) mirror for improved spatial access. Image taken from Shoppell et al. [70]

Table 3.2: A summary of the optical/experimental components used for the modified z-type schlieren setup.

Optical Component	Part	Quantity	Focal Length (mm)
Focusing Lens	Thorlabs AC508-150-A ⌀2”	1	150
Parabolic Mirror	J. Unertl Optical Co. ⌀12”	2	2457.45
Knife-Edge Cutoff	Dewalt DWHT11131L	1	N/A
Camera Lens	SIGMA f/2.8 EX DG HSM OS	1	70-200
Camera	Photron FASTCAM SA-Z	1	N/A

Catch Side

The collimated light passes through the test section and hits the second parabolic mirror (f_L = 96.75 in). The parabolic mirror focuses the light until it hits a folding (flat) mirror located about 60 in away. The folding mirror provides additional space for optical access. The folding mirror provides additional space for camera placement. The folding mirror reflects the light, and the light continues to focus. The knife-edge cutoff is inserted at the focus associated with vertical density changes. The light then passes into the camera lens and is focused onto the camera sensor.

3.1.3 Pressure Transducers

Two pressure transducers were installed in the flat plate to investigate the spectral content of the boundary layer without a hemicylindrical blunt-fin installed. In order to prevent contamination of the underlying flow physics (potential wake generation), the transducers were installed on opposite sides of the centerline. The pressure transducers were installed 25.4 mm and 79.4 mm from the leading edge of the plate and will be referred to as the upstream and downstream transducers, respectively. The upstream pressure transducer was a Kulite XCQ-SL-062-15A ultraminiature pressure transducer [43], and the downstream pressure transducer was a Kulite XCS-062-10A high-sensitivity ultraminiature pressure transducer [44]. Both transducers were connected to a Kulite KSC-2 high performance signal conditioner [42] to amplify the voltage signals. A summary of pertinent transducer characteristics is displayed in Table 3.3 below.

3.2 Analytical Methodology

3.2.1 Shock Tracking

Schlieren is typically a qualitative technique; however, recent advances in high-speed imaging and image processing now allow for quantitative values to be extracted from raw images. In the past, intrusive techniques such as pressure taps were required to provide insight into the unsteady behavior occurring within the separation region. Now with the rapid technological

Table 3.3: A summary of the Kulite pressure transducer characteristics.

Kulite Pressure Transducer	XCQ-SL-062-15A	XCS-062-10A
Pressure Range [psia]	15	10
Resolution	Infinitesimal	Infinitesimal
Sensitivity* [psia/V]	1.48192	0.80058
Combined Error (Typ.)	±0.1% FSO BFSL	±0.1% FSO BFSL
Combined Error (Max.)	±0.5% FSO	±0.5% FSO
Natural Frequency w/o Screen [kHz]	200	175
*Sensitivity after signal conditioning		

advances in high-speed camera technology and image-processing, more precise measurements can be extracted from imaging. To obtain these measurements, a shock tracking algorithm was designed in MATLAB to record the dynamic movement of the separation shock foot (defined in Fig. 2.2).

This shock tracker was designed as a "streaming" process to reduce the amount of RAM used by the MATLAB workspace. Streaming is a process in which calculations are performed on an image-by-image basis. For this code, a single image is imported to the workspace before image operations begin. Next, the image is flipped from left-to-right to ensure the flow follows standard convention, and then rotated so the axes of the image align with the wall-normal and streamwise directions. The image is now cropped to only include from the leading edge of the plate to the face of the hemicylindrical blunt-fin.

The crux of this technique is the binarization process. As previously discussed, schlieren images show the spatial variations in density of a given flowfield, and with the use of digital sensors, these variations can be assigned an intensity value for each individual pixel. A near instantaneous jump in the density of a fluid is a fundamental characteristic of a shockwave, and therefore the shock structures appear as incredibly strong features in schlieren images. This is leveraged in MATLAB [77] through the use of the *imbinarize* function.

The *imbinarize* function by default uses a 256-bin histogram from the complete image to calculate Otsu's threshold for global binarization [59, 76]. However, due to the large amount variance throughout the density of the flowfield, a more localized method was required. The adaptive option was chosen for *imbinarize* as it calculates a local threshold for each pixel using Bradley's method [5, 76]. In addition, the adaptive option uses a neighborhood size that is approximately 1/8 of the image size for this method. The foreground polarity was set to dark to ensure that the darkest features, such as shockwaves, in the image were not removed by the threshold function. The sensitivity factor was set to a value of 0.09 which means that all features less than or equal to the 9th-percentile of intensity values in the image were preserved. An example of this threshold-bounded binarization technique is presented in Fig. 3.5 below.

After the image was set to a binary state, the shockwave position was investigated. A 26 x 26 pixel region of interest around the interaction region was used for tracking the

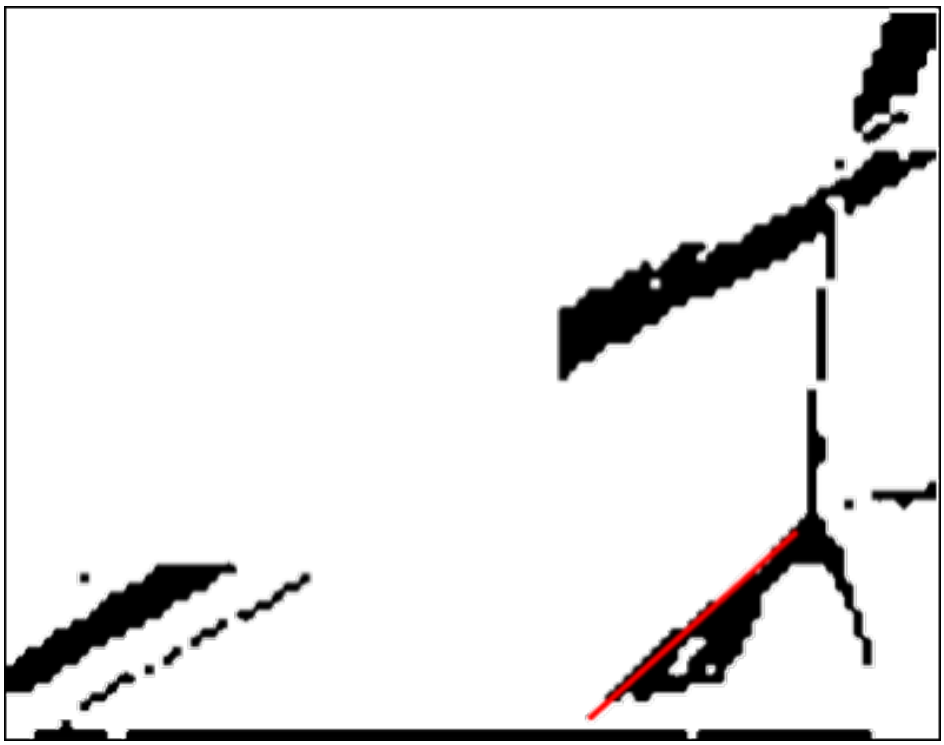

(a) Threshold-bounded Binarized Image w/ Shock Tracker Overlay

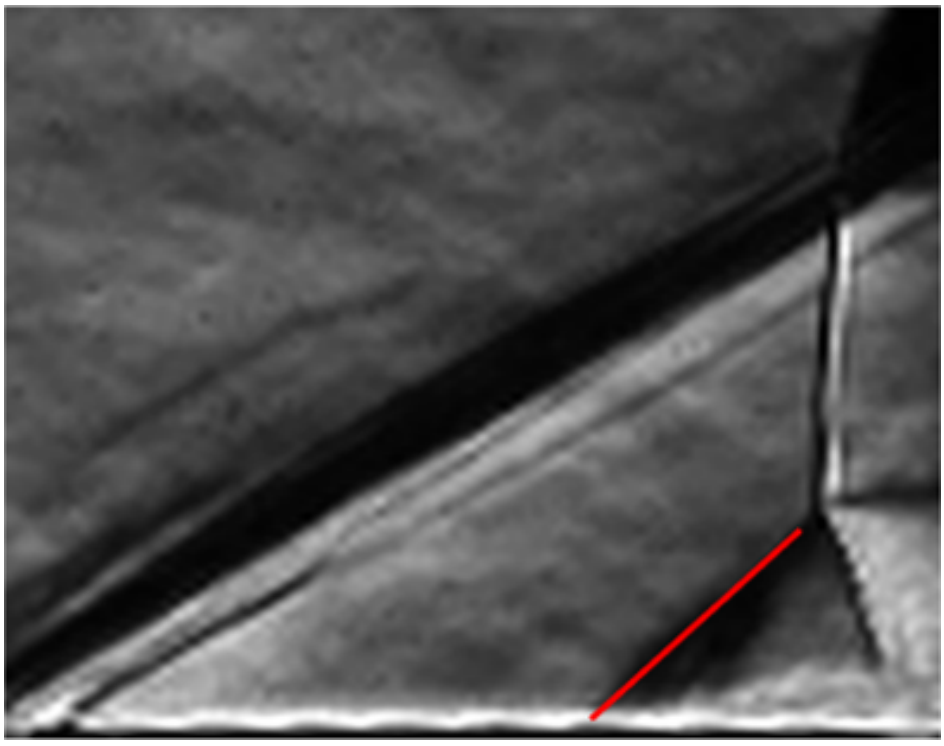

(b) Schlieren image w/ Shock Tracker Overlay

Figure 3.5: A comparison of the shock tracker overlaid onto both a binarized image and a schlieren image. NOTE: The waviness present near the bottom of the schlieren image is an artifact of the image rotation process.

shockwave position. An array of row and column locations is extracted from the image and used to calculate the slope of the shockwave position. The slope is used with one of the previously calculated locations to extrapolate to a pre-determined wall normal location. The extrapolation does introduce some uncertainty as the shockwave will refract within the boundary layer, however, due to the thin nature of the boundary layer in this experiment ($\delta < 1$ mm) the uncertainty is relatively negligible. This extrapolation is recorded as the shock foot position, and then the process repeats for a new image until the entire data set is processed. The accompanying code for this section can be found in the appendices.

3.2.2 Zero-Crossing Frequency

The zero-crossing rate, ZCR, is a boxcar approach to predicting the rate at which a signal passes over a given value. The boxcar approach binarizes the signal, $x(t)$, into a positive or negative sign value, $s(t)$ (see Eq. 3.4). The summation of sign changes is divided by two times the signal length, T, to give the zero-crossing rate. This work calculated the zero-crossing rate using the *zerocrossrate* function in MATLAB [77].

$$ZCR = \frac{1}{2T}\sum_{t=2}^{T}|s(t) - s(t-1)| \tag{3.3}$$

where:

$$s(t) = \begin{cases} 1 & x(t) \geq 0 \\ -1 & x(t) < 0 \end{cases} \tag{3.4}$$

In order to calculate the zero-crossing frequency, f_{zc}, ZCR is multiplied by the Nyquist frequency, $f_s/2$ (see Eq. 3.5).

$$f_{zc} = ZCR \times \frac{f_s}{2} \tag{3.5}$$

3.2.3 Probability Density Function

The probability density function (PDF) is the relative likelihood that a random data sample will fall within a specific range of values. Typically, the x-axis of a PDF is displayed in standard deviations, however, it was plotted as the nondimensional distance (x/d) from the face of the blunt-fin to provide a physical understanding of the λ_1 shock behavior. The

PDFs for the standoff distance of the λ_1 shock foot for each data set were calculated using the *histogram* function in MATLAB. A histogram bin width of 0.05 was used for all data sets for consistency.

3.2.4 Power Spectral Density

The power spectral density (PSD) is defined as the discrete-time Fourier transformation (DTFT) of the autocorrelation function [73]. The PSD provides the average signal power distribution per each frequency. As the properties of the Fourier transform require an infinitely long data set, approximations must be made in order to calculate an estimate of the PSD. A popular choice of estimation methods, used in this work, is Welch's method [85]. Welch's method is an adaptation of Bartlett's method, but varies in two main ways. First, Welch's method allows the overlap of data segments whereas Bartlett's method does not. Second, each data segment is windowed, a Hanning window was used in this work, before an estimate of the periodogram can be computed.

Equation 3.6 defines the jth data segment where the time, t, goes from 1 to the number of samples in each data segment, M. The overlap of each data segment, K, is defined by user input. The recommended overlap by Welch [85] is 50%, thus the overlap is $K = 0.5M$. A 50% overlap was used in this work. The number of data subsamples within each data set, S, is equivalent to the total number of data samples, N, per overlap ($S = N/K \simeq 2N/M$) [73]. Please note that the equation referenced in Stoica is written incorrectly as N and M were accidentally switched.

$$y_j(t) = y((j-1)K + t), \qquad \begin{matrix} t = 1, ..., M \\ j = 1, ..., S \end{matrix} \tag{3.6}$$

The windowed periodogram, $\hat{\phi}_j(\omega)$, is computed for each data segment using Eq. 3.7.

$$\hat{\phi}_j(\omega) = \frac{1}{MP}\left|\sum_{t=1}^{M} v(t)y_j(t)e^{-i\omega t}\right|^2 \tag{3.7}$$

The power, P, is computed over the temporal window, $v(t)$, in Eq. 3.8 and plugged back into Eq. 3.8.

$$P = \frac{1}{M} \sum_{t=1}^{M} |v(t)|^2 \tag{3.8}$$

To obtain Welch's estimate of the PSD, $\hat{\phi}_W(\omega)$, the windowed periodograms are averaged using Eq. 3.9.

$$\hat{\phi}_W(\omega) = \frac{1}{S} \sum_{j=1}^{S} \hat{\phi}_j(\omega) \tag{3.9}$$

For this experiment, the data was mean subtracted to ensure that the data is wide-sense stationary. This allows the autocorrelation function to be equivalent to the variance of the data as any phase shift is eliminated. Thus when the PSD estimate (now defined as G_{xx}) is calculated, the area under the curve will be equivalent to the variance. The PSD estimation using Welch's method was used using the *pwelch* command in MATLAB. This command, shown in Eq. 3.10, was used with the following inputs: mean subtracted data ($x - \bar{x}$), a Hann window with a length of 2^{10} points, a 50% window overlap (512 points), 2^{10} discrete Fourier transform (DFT) points, and the camera sampling frequency, f_s, of 100 kHz. These inputs yielded a frequency resolution, df, of ~97.7 Hz. The *pwelch* command output the PSD estimate and the corresponding frequencies, f.

$$[G_{xx},\ f] = pwelch(x - \bar{x}, window(L), overlap, nfft, f_s) \tag{3.10}$$

3.3 Error and Uncertainty

Combs et al. [14] and Lash et al. [47] defined the width of the separation shock as the largest source of uncertainty in their shock tracker. As the shock tracker used in this code is based on similar coding techniques, this holds true in this work as well. The uncertainty, quantified by Eq. 3.11, estimates the change in the non-dimensional separation shockwave location in any given frame. The uncertainty of the shock thickness in meters is defined as Δx_{sep}, d is the diameter of the cylinder in meters units, s is the visual shock thickness in meters, and N is d represented in terms of pixels. The spatial resolution for this work was 0.1728 mm/pixel.

$$\frac{\Delta x_{sep}}{d} \approx \sqrt{\frac{s^2}{d^2} + \frac{1}{N^2}} \tag{3.11}$$

Using Eq. 3.11, the uncertainty was found to be $\pm 5.1\%$ ($\pm 0.2d$). All values greater than 3σ from the mean location were determined to be erroneous and set to NaN. In addition, all locations that occur downstream of the ROI are set to NaN. Approximately 2.5% of 20,000 frames were found to be erroneous. Any frames with missing x-locations were assigned a value using the MATLAB *fillmissing* function which linearly interpolates using the neighboring data points. Due to the low-level of erroneous frames, the error produced from interpolation is not expected to affect the probability density functions or power spectral density estimates.

Chapter 4

Results and Analysis

This chapter discusses the results of this experimental work. First, the results of the pressure transducer investigation of the boundary layer are discussed. Subsequently, the impact of reducing the interaction strength on the scaling of the transitional shockwave boundary layer interaction (XSBLI) is analyzed, emphasizing the XSBLI statistical moments and the mean interaction structure. Finally, the correlation between the interaction strength and the low-frequency unsteadiness in the separation region will be addressed.

4.1 Boundary Layer Investigation

The experimental investigation of two streamwise locations, 25.4 mm and 79.4 mm, from the leading edge, with Kulite pressure transducers indicated the presence of the narrowband freestream noise in the boundary layer at the upstream probe location (see Fig. 4.1a). The spectral content is comparatively weaker than the content measured in the freestream, but is still clearly centered at a similar frequency. The spectral content evolves into a more broadband shape in the downstream Kulite (see Fig. 4.1b). The coherence, $C_{xy}(f)$, was calculated between the mean-subtracted signals of the upstream and downstream Kulites for each individual run (see Fig. 4.2). The strongest coherence was observed for $f < 2$ kHz with low-levels of coherence observed in the region of interest. There were local maxima observed between $3 - 5$ kHz, but with coherence levels < 0.15 it was deemed this content was inconclusive.

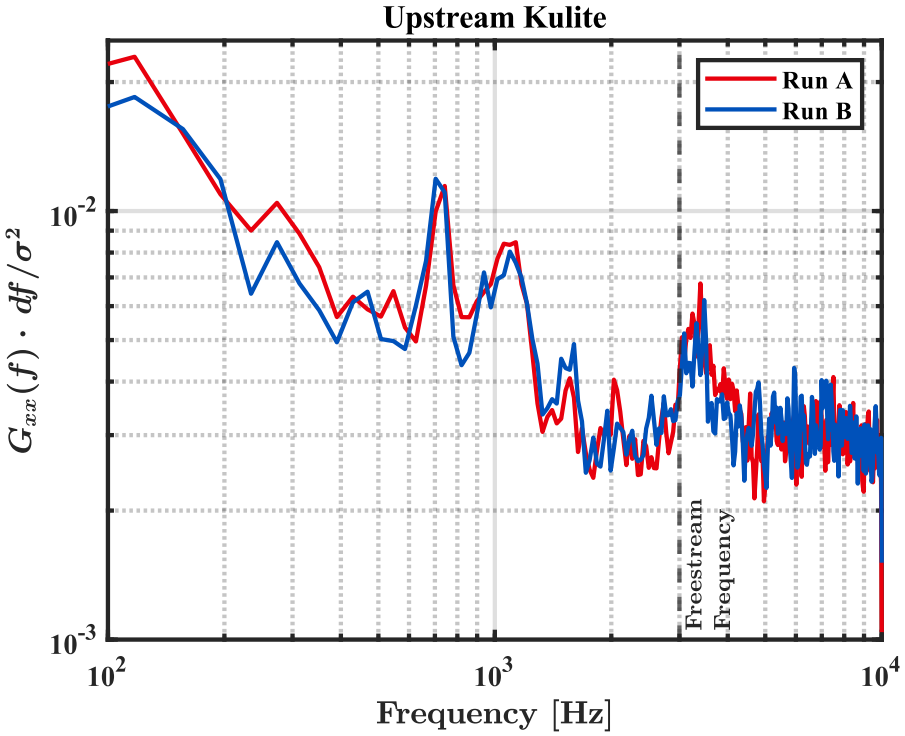

(a) PSD of upstream Kulite located 25.4 mm ($x/d = 8$) from the leading edge.

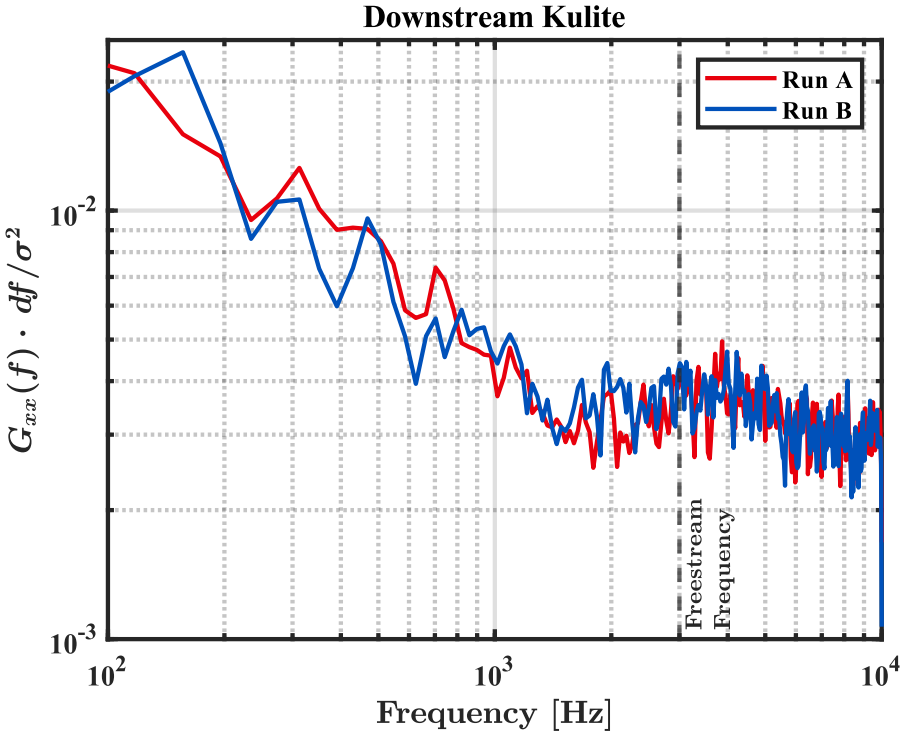

(b) PSD of downstream Kulite located 79.4 mm ($x/d = 25$) from the leading edge.

Figure 4.1: The streamwise development of spectral content recorded with pressure transducers.

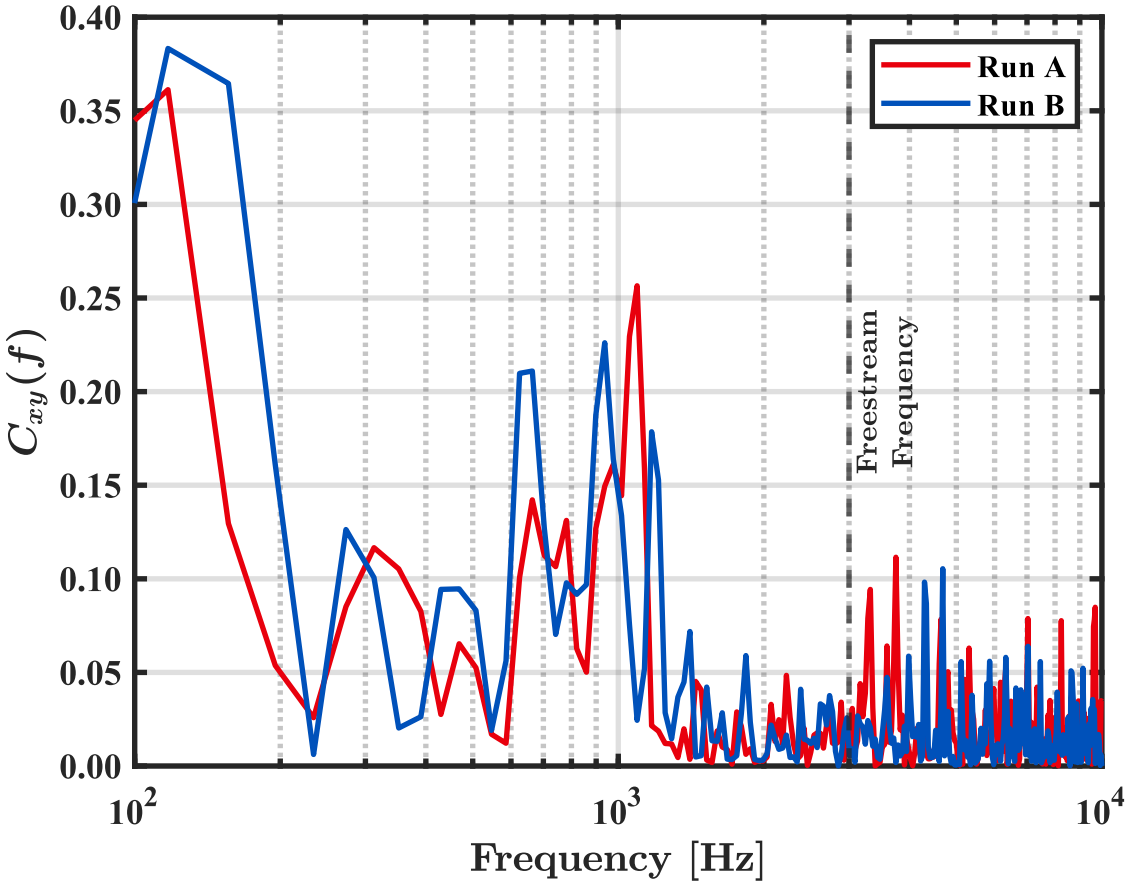

Figure 4.2: Mean-Squared Coherence of the upstream Kulite to downstream Kulite for runs A and B, respectively. NOTE: This plot is only logarithmic on the x-axis.

4.2 Scaling of Interaction with Shock Strength

The mean of 20,000 schlieren images was calculated for all sweep angles and are shown in Fig. 4.3 below. As predicted by high-speed viscous theory in Hirschel [31], the average shock standoff distance and mean separation bubble size decreased with a reduction in shock strength. The magnitude of the adverse pressure gradient decreases inversely with the sweep angle, thus decreasing the strength of the feedback mechanism [41, 87, 31]. Figure 4.4 shows the probability density function (PDF) of the shock standoff distance for each sweep angle and further exemplifies the reduction in the scale with the reduction in shock strength. In order to properly understand the PDF content, the statistical moments were calculated for each sweep angle (see Table 4.1). The 0° sweep case exhibits the largest range of standoff distances with a mean location, $\mu_{\lambda_1/d}$, occurring at approximately $2.3d$ upstream of the cylinder which shows excellent agreement with the location reported by Lash et al. [47]. The standard deviation, $\sigma_{\lambda_1/d}$, was $\sim 0.23d$ or $\sim 9.9\%$ of $\mu_{\lambda_1/d}$. The skewness, $\tilde{\mu}_{3,\lambda_1/d}$, of the 0° case is about -0.72 which indicates that the shock foot location is "left-skewed", or in a more physical sense, upstream-skewed. This suggests a combination of a higher-range, but lower-probability of shock locations upstream of μ_{λ_1}. The kurtosis, $\tilde{\mu}_{4,\lambda_1/d}$, indicates the separation shock foot in the unswept case behaves in a leptokurtic manner $\left(\tilde{\mu}_{4,\lambda_1/d} \approx 5.09\right)$ implying a higher probability of outliers occurring and a larger amount of deviation near the mean. In another sense, this indicates that the distribution of unsteadiness in the flowfield is closer to a Laplacian distribution than a Gaussian one.

The 10° sweep case in Fig. 4.4 illustrates the shock foot is less likely to deviate from a mean location of $\mu_{\lambda_1/d} \approx 2.1d$ than the unswept case $\left(\sigma_{\lambda_1/d} \approx 0.15d\right)$. This indicates that the unsteady movement of the separation shock and the length of the interaction was reduced as expected with an increase in sweep angle. The 10° case also showed a significant decrease in the skewness of the data, but the interaction PDF was still classified as upstream-skewed. The kurtosis of the PDF indicated an even stronger leptokurtic distribution $\left(\tilde{\mu}_{4,\lambda_1/d} \approx 5.36\right)$ than the unswept case. This implies that although the probability the shock foot is present at the mean location is much higher, the likelihood of outliers appearing in the interaction is much higher as well.

Table 4.1: Statistical moments for all sweep angles. The mean, standard deviation, and variance have all been non-dimensionalized in terms of x/d.

Sweep Angle	$\Lambda = 0°$	$\Lambda = 10°$	$\Lambda = 20°$	$\Lambda = 30°$
$\mu_{\lambda_1/d}$	-2.314	-2.092	-1.569	-1.164
$\sigma_{\lambda_1/d}$	0.234	0.145	0.230	0.046
$\sigma^2_{\lambda_1/d}$	0.055	0.021	0.053	0.002
$\tilde{\mu}_{3,\lambda_1/d}$	-0.722	-0.400	0.442	-0.137
$\tilde{\mu}_{4,\lambda_1/d}$	5.088	5.363	4.759	4.509

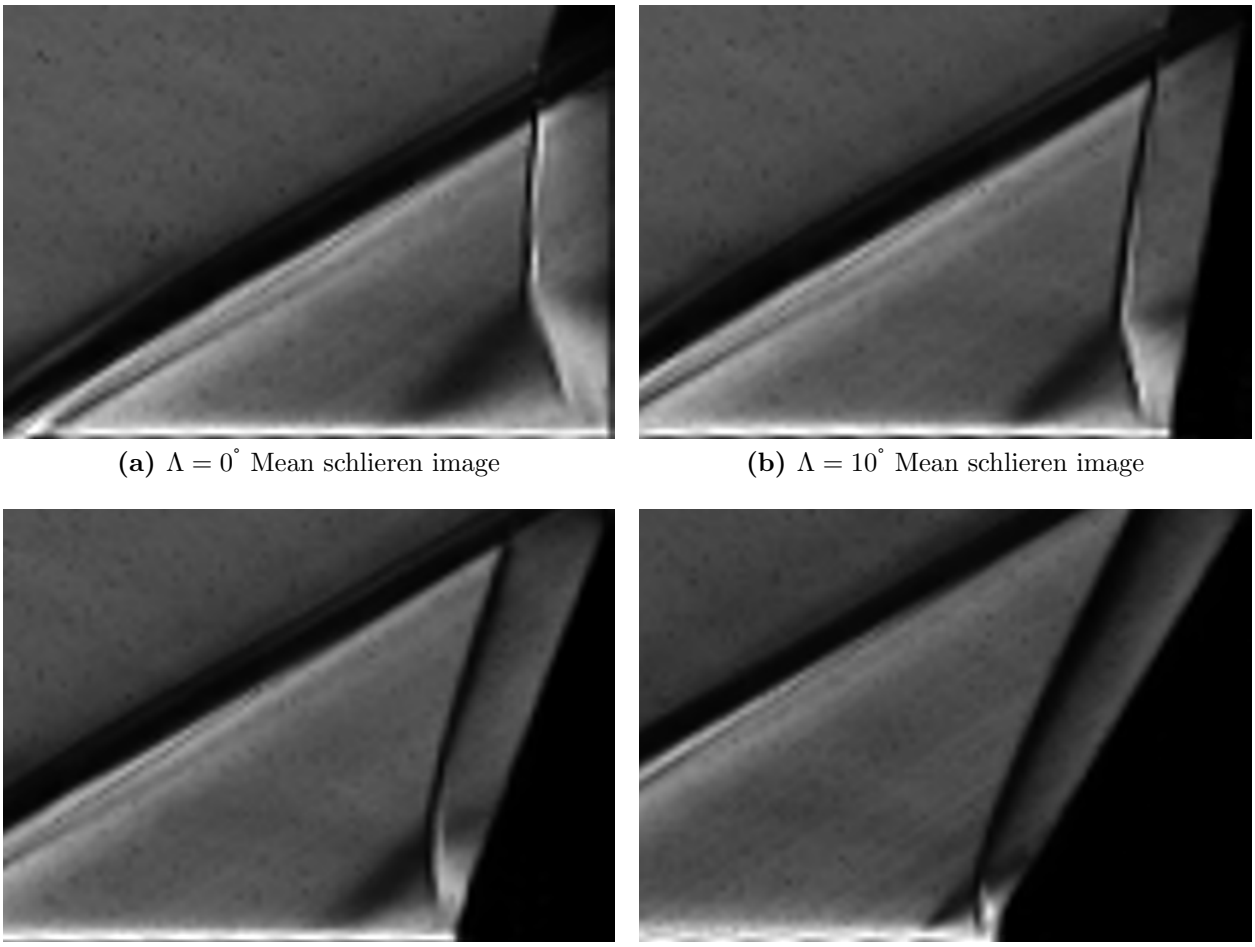

(a) $\Lambda = 0^{\circ}$ Mean schlieren image

(b) $\Lambda = 10^{\circ}$ Mean schlieren image

(c) $\Lambda = 20^{\circ}$ Mean schlieren image

(d) $\Lambda = 30^{\circ}$ Mean schlieren image

Figure 4.3: The mean schlieren images for all sweep angles are shown to illustrate the collapse of the interaction scale as the sweep angle is increased. Image taken from Shoppell et al. [70] with permission from the American Institute of Aeronautics and Astronautics.

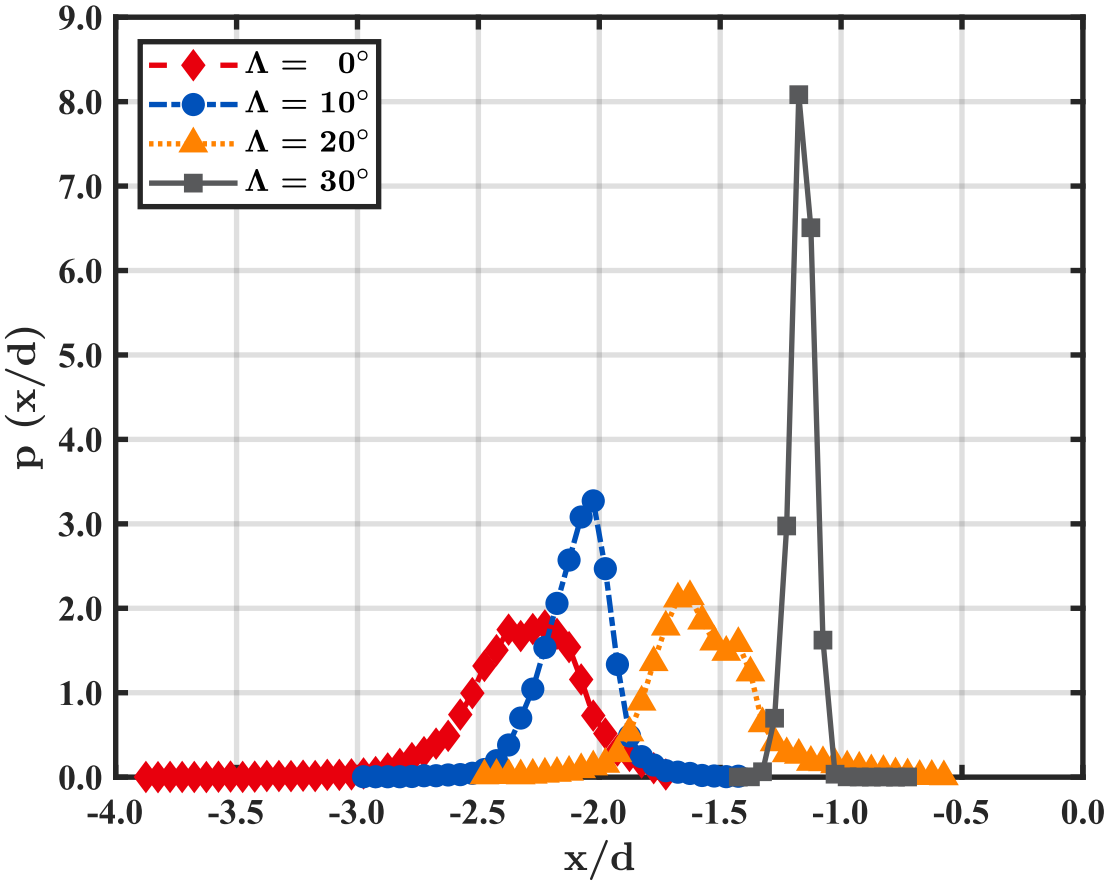

Figure 4.4: Standoff distance PDF for all sweep angles. Image taken from Shoppell et al. [70] with permission from the American Institute of Aeronautics and Astronautics.

In the 20° case the mean location decreases by about $0.5d$ from the 10° configuration; however, $\sigma_{\lambda_1/d}$ increased to $0.23d$ similar to the value of the unswept case. The 20° case is the only configuration with a "right-skewed" or downstream-skewed PDF $\left(\tilde{\mu}_{3,\lambda_1/d} \approx 0.44\right)$. This suggests that a mechanism such as the mass-entrainment of the separation bubble could be much weaker than the first two configurations, and consequently, the incoming boundary layer momentum has the potential to push the bubble farther downstream. The kurtosis of the 20° configuration is still leptokurtic $\left(\tilde{\mu}_{3,\lambda_1/d} \approx 4.76\right)$, but is less so than the other configurations. Thus, there is still a high chance of outliers in the data.

The probability of the 30° case to remain near a mean location of $1.1d$ is approximately four times higher than the 0° sweep case (see Fig. 4.4). In addition, the standard deviation is reduced by an order of magnitude from the other configurations $\left(\sigma_{\lambda_1/d} \approx 0.04\right)$. The 30° configuration has significantly less skewed data, but is slightly upstream-skewed again $\left(\tilde{\mu}_{3,\lambda_1/d} \approx -0.14\right)$. As expected from the other cases, the PDF possesses a leptokurtic distribution; however, with a $\tilde{\mu}_{3,\lambda_1/d} \approx 4.51$ and a low level of skewness, the distribution is roughly halfway between a Gaussian and Laplacian distribution.

The zero-crossing frequencies, f_{zc}, are displayed at 25 evenly-spaced streamwise locations for all sweep angles in Fig. 4.5. The 0° blunt-fin distribution of f_{zc} agrees extremely well with the distribution reported by Combs et al. [11] with a $f_{zc} \approx 12$ kHz. The maximum zero-crossing frequency for the 10° case increases by roughly 10 kHz to ∼17 kHz. This was expected due to the smaller standard deviation in the distribution of separation shock locations in this configuration. The 20° case exhibited a peak $f_{zc} \approx 21$ kHz, nearly double the zero-crossing frequency of the unswept configuration. The 30° configuration shows a relaxation of f_{zc} to about 18 kHz.

The streamwise intermittency of the separation shock, γ_{λ_1}, is displayed at 25 evenly-spaced streamwise locations for all sweep angles in Fig. 4.6. The maximum upstream location of $x/d = -3.89$ in the 0° blunt-fin intermittency, x_{λ_1} ($\gamma_{\lambda_1} = 0$), agrees exceptionally well with the values reported by Combs et al. [11]. However, the increase in sweep angle reduces the upstream distance needed to reach zero intermittency. Furthermore, the 10° case exhibits a steeper slope near the mean location of the interaction, once again suggesting that outliers are more likely to occur in this interaction. As expected from the similarity

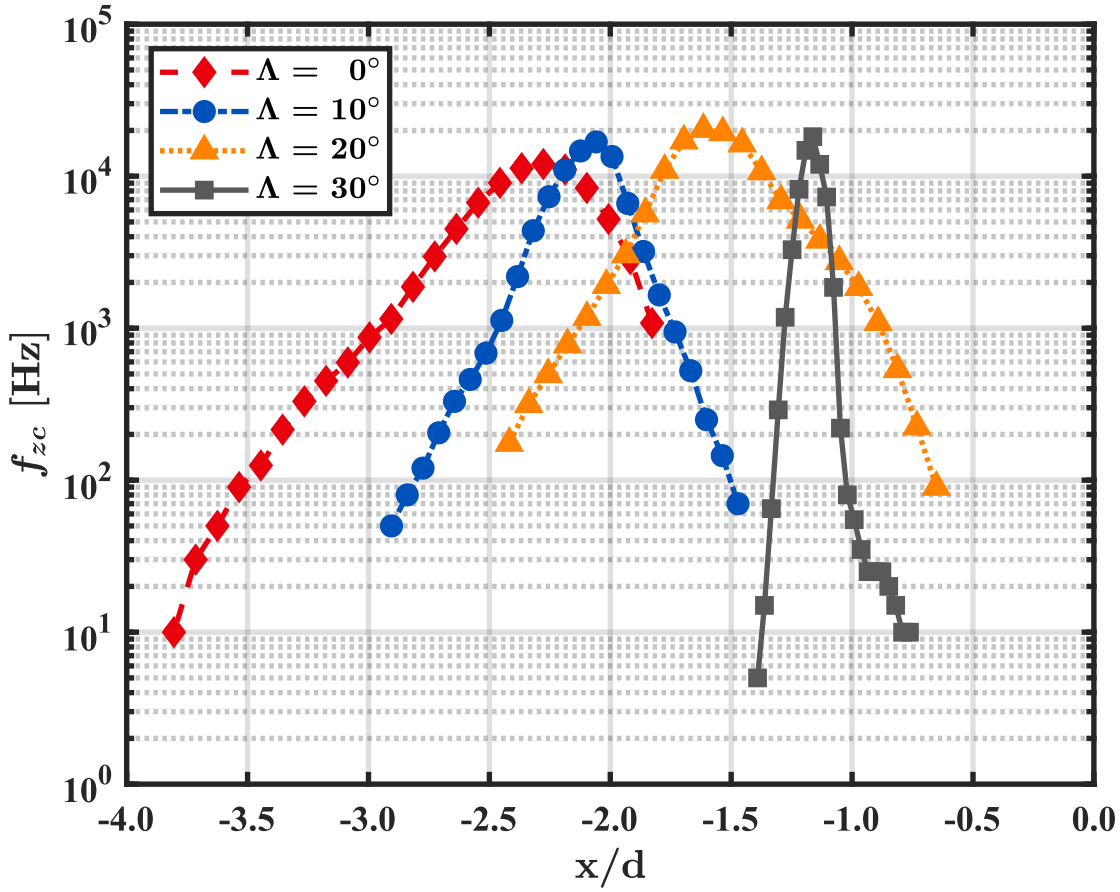

Figure 4.5: Zero-crossing frequencies at different streamwise locations for all sweep angles. NOTE: Only the y-axis is logarithmic.

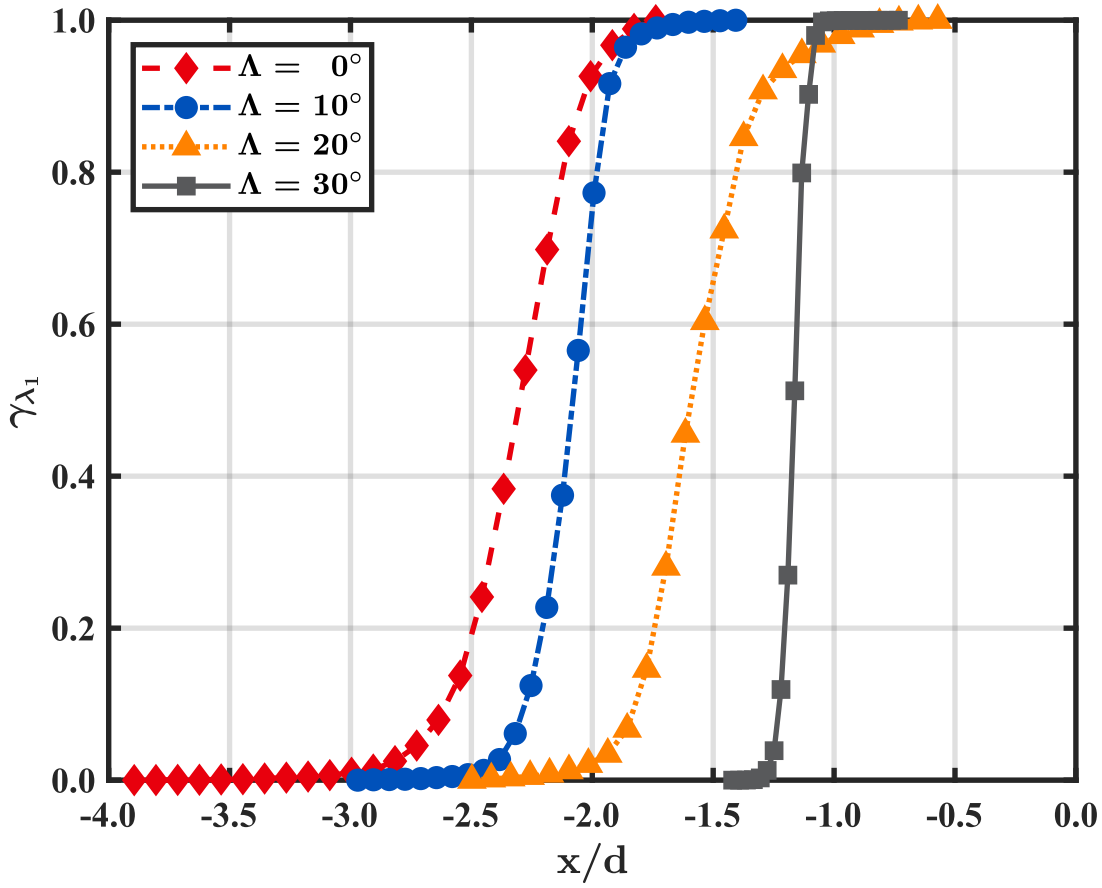

Figure 4.6: Intermittency of separation shock foot at different streamwise locations for all sweep angles.

reported in the statistical moments, the intermittency distribution for the 20° case shows good agreement with the unswept case, albeit at a smaller scale. Lastly, the 30° case has the steepest slope and, consequently, the smallest distribution of the intermittency function, which agrees with the small distribution of separation shock locations in the corresponding PDF.

The relative shock strength is shown in Fig. 4.7. Although shock strength has been defined several different ways, this work defines the shock strength using the Korkegi turbulent separation parameter, $M_1\theta_i$ (defined by Eq. 4.1), as a metric for "strength." The relative shock strength (see Eq. 4.2) was defined as the ratio of the Korkegi parameter at a blunt-fin sweep angle, Λ, to the Korkegi parameter for the unswept ("strongest") case. The strength of the interaction was shown to quickly decrease with an increase in sweep angle as expected. The 10° case exhibited approximately a 17% reduction in relative shock strength. Another 10% reduction in the relative shock strength occurred in the 20° case bringing the shock strength to about 72% of the unswept configuration. However, the 30° case remained at approximately the same value of 72%, thus suggesting a potential lower limit for relative shock strength in blunt-fin-generated interactions.

$$M_1\theta_i = \frac{M_n^2 - 1}{\left(\frac{\gamma+1}{2}\right) M_n} \tag{4.1}$$

Taking the ratio of the interaction sweep angle to the unswept shock strength yields:

$$\text{Relative Shock Strength} = \frac{M_1\theta_i(\Lambda)}{M_1\theta_i(\Lambda = 0°)} \times 100\% \tag{4.2}$$

4.3 Scaling of Interaction Dynamics with Shock Strength

4.3.1 Power Spectral Density of Separation Shock Position Values

The following subsection was adapted with some revisions from Shoppell et al. [70]. The normalized spectra results for the hemicylindrical blunt-fin are shown in Fig. 4.8. The PSD was normalized by dividing the raw spectra by the variance, σ^2, and multiplied by the change in frequency, df. This normalization scheme allows for the relative shape and

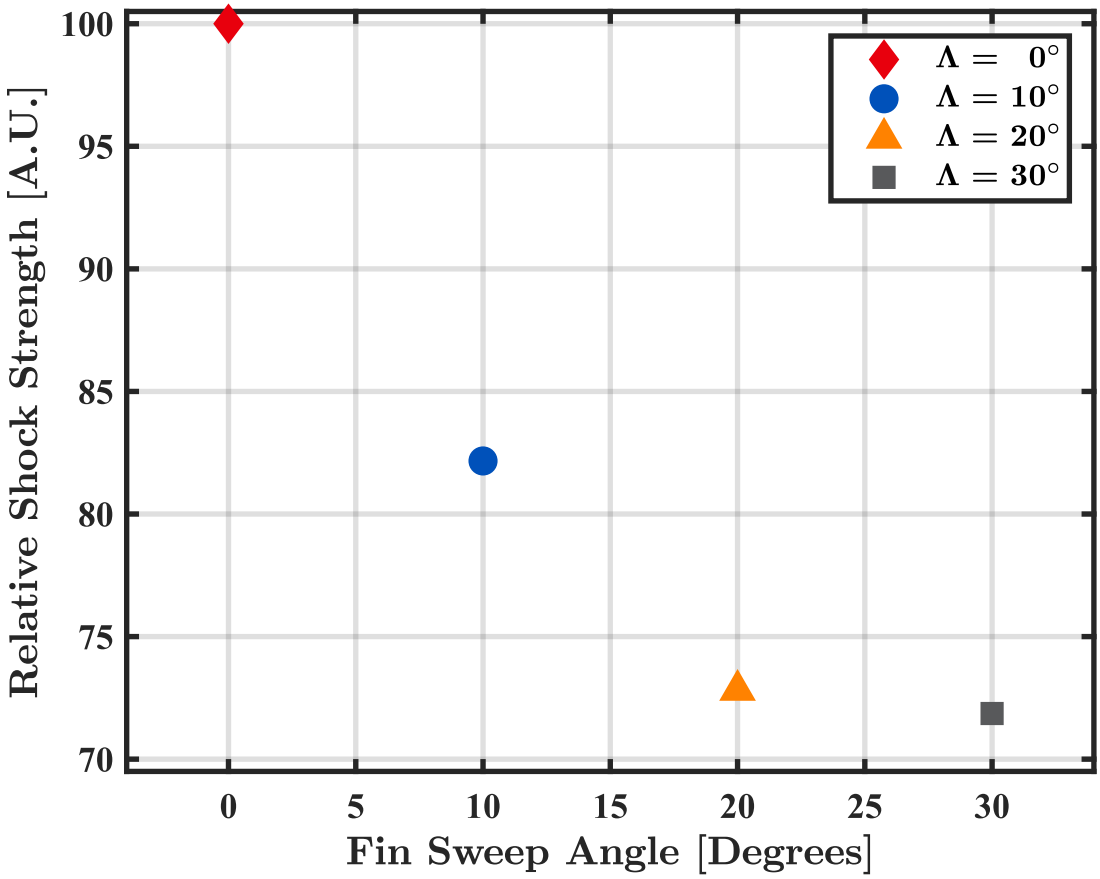

Figure 4.7: Relative shock strength at all sweep angles.

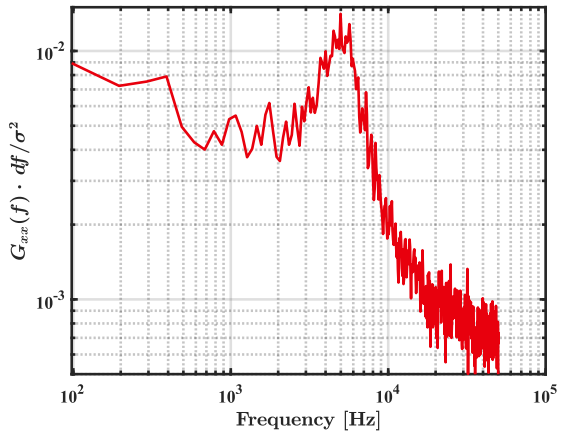

(a) The normalized power spectra results for $\Lambda = 0°$

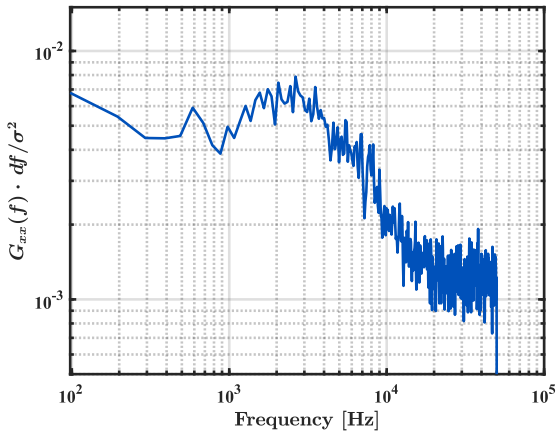

(b) The normalized power spectra results for $\Lambda = 10°$

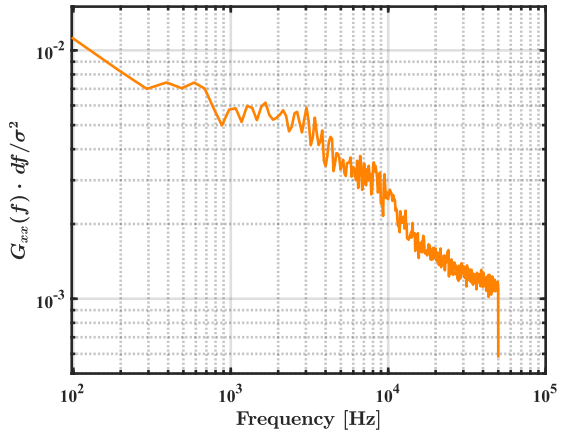

(c) The normalized power spectra results for $\Lambda = 20°$

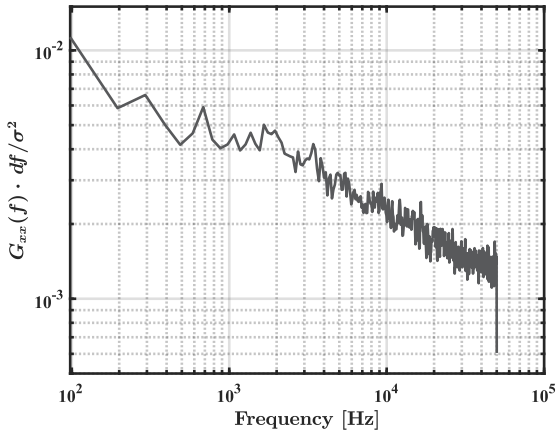

(d) The normalized power spectra results for $\Lambda = 30°$

Figure 4.8: Normalized power spectral densities measured from schlieren images for each sweep angle. Image taken from Shoppell et al. [70] with permission from the American Institute of Aeronautics and Astronautics.

behavior of multiple spectra to be directly compared. The same peak in the spectral content, ∼5 kHz, that was reported by Lash et al. [48, 47, 45, 46] and Combs et al. [14, 10, 11, 15] is present in the unswept case (see Fig. 4.8a). However, the bandwidth of the peak in this experimental campaign is slightly broader, but this is likely due to slight changes in experimental conditions. The PSD results for the $\Lambda = 10^{\circ}$ swept fin, shown in Fig. 4.8b, did not produce the resonant behavior observed in the unswept case. Nevertheless, a broad peak in the spectra is still visible and centered around ~ 2.5 kHz. The shape of the spectra, in addition to the lower standoff distance and standard deviation shown in Fig. 4.4, indicates the XSBLI is beginning to bias towards the limiting turbulent state. In the $\Lambda = 20^{\circ}$ case, shown in Fig. 4.8c, the broadband behavior is significantly lower in amplitude than the $\Lambda = 10^{\circ}$ case. However, as shown in Fig. 4.8d, in the $\Lambda = 30^{\circ}$ case the roll off rate of the high frequency content decreases. For this case, the PSD indicates that the unsteadiness within the interaction is weak and the SBLI has developed to a quasi-steady state.

Figure 4.9 shows the power spectral densities from Fig. 4.8 non-dimensionalized by f instead of df. This allows the relative spectra roll off to be compared by offsetting them, and is consistent with the way some promiment prior research groups have published their reported spectra. It is clearly seen that the slope of the high-frequency roll off for frequencies greater than 10 kHz is very similar between the $\Lambda = 10^{\circ}$ and $\Lambda = 20^{\circ}$ cases. This suggests that as the shock strength decreases, the relative behavior of the higher-frequency shock content is unaffected. The work of Erengil and Dolling [25] and Dolling and Or [23] reinforces this as they found the high-frequency content to be caused by large turbulent structures upstream of the interaction and to be dependent on the incoming boundary layer thickness.

4.3.2 Power Spectral Density of Image Intensity Values

In order to illustrate the decrease in narrowband unsteadiness as sweep angle is increased, average power spectral density images were calculated using Eq. 4.3 for all sweep angles. Each case was integrated across a 2 kHz frequency band that encompasses the strongest low-frequency content at each sweep angle. For the unswept case with a peak at ~ 5 kHz, the data was integrated from 4 kHz to 6 kHz. The 10° swept fin was integrated from 1.5 kHz to 3.5 kHz to capture the broadband behavior centered at ~ 2.5 kHz. All other sweep angles

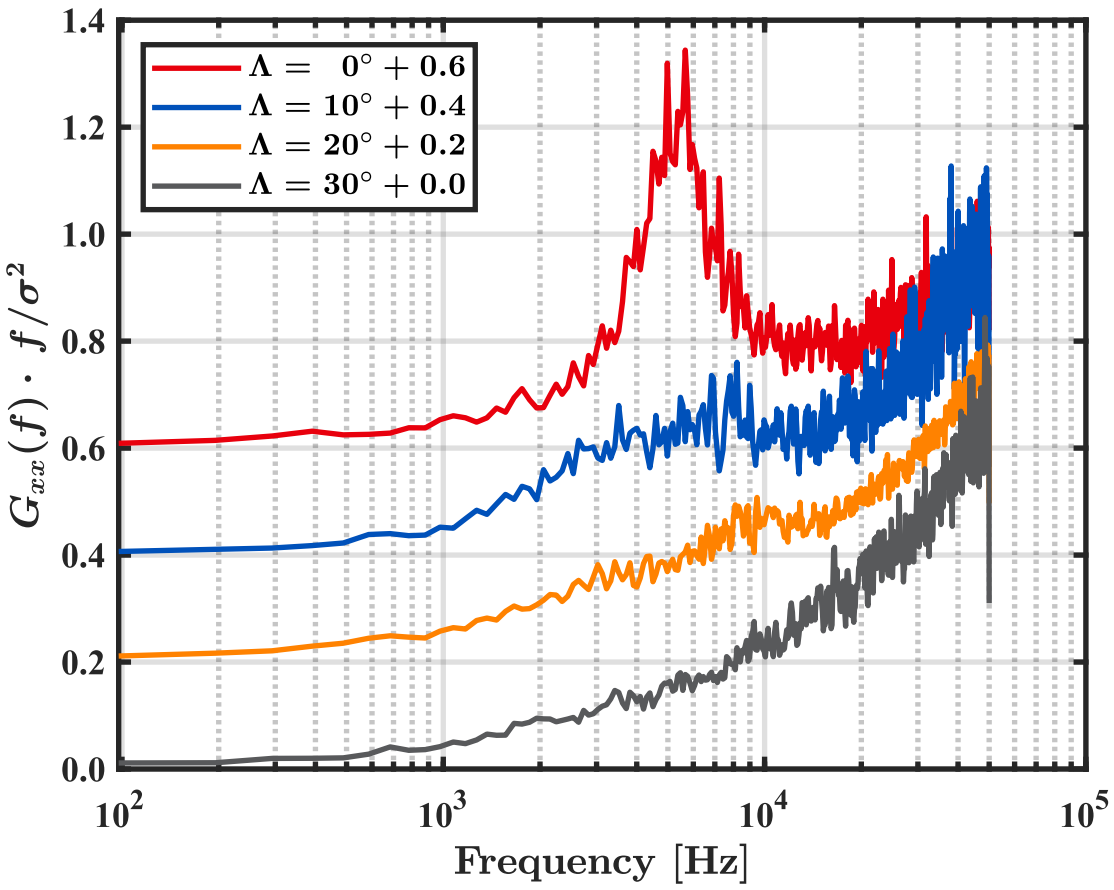

Figure 4.9: Offset pre-multiplied power spectral density distribution as a function of sweep angle. Image taken from Shoppell et al. [70]

were integrated between 1.5 kHz to 3.5 kHz to illustrate the relaxation of the low-frequency content.

$$\frac{G_{xx}\Delta f}{\sigma^2} = \int_{f_1}^{f_2} \left(\frac{G_{xx}}{\sigma^2}\right) df \tag{4.3}$$

As expected from the PSD for the unswept case, the interaction region in Fig. 4.10b exhibits high-amplitude spectra between 4-6 kHz. From this image, it can be seen that the unsteadiness in the interaction is not only present in the separation shock foot, but in the movement of the triple-point jet as well. The unsteadiness of the triple point indicates an inherent bias towards the reattachment region. The high-frequency content present just behind the mean λ_1 structure indicates a high level of unsteadiness in other features of the separation region. This could be due to the flapping of the separating shear layer that was observed by Hoffman et al. [32] and Cottier et al. [16], or a product of the tone amplification and feedback mechanism suggested by Pirozzoli and Grasso [61]. The upstream-influence (UI) shock also displays some unsteadiness in the 4-6 kHz range albeit at a relatively lower level of average spectral content $\left(\sim \frac{1}{3} \times \frac{G_{xx}\Delta f}{\sigma^2}\right)$ than the unsteadiness in the interaction region.

The reduction of shock strength was shown to greatly reduce the low-frequency unsteadiness within the interaction. Fig. 4.10a indicates that the unsteadiness in a 2 kHz band around f_{max} was reduced by roughly $33\% - 50\%$ for the $\Lambda = 10^\circ$ case. As observed by Gonsalez and Dolling [30], the reduced interaction strength, and consequently the weakened downstream mechanism, have a large impact on the unsteadiness of the separation shock foot. There is no longer a UI shock present in the interaction. The reduction of shock strength, which consequently reduced the length of the separation bubble, appears to have eliminated, or at least greatly reduced, the presence of a UI shock from the flowfield. The spectral content in the 20° case (Fig. 4.10a) shows reasonable agreement to the 10° case albeit at lower average spectral content. The 30° case in Fig. 4.10a highlights the low levels of unsteadiness in the interaction region relative to the other sweep angles. Also of note in Fig. 4.10 is the relative PSD strength observed in the leading edge shockwave in relation to the freestream. Davenport and Gragston [18] measured similar high-amplitude narrowband

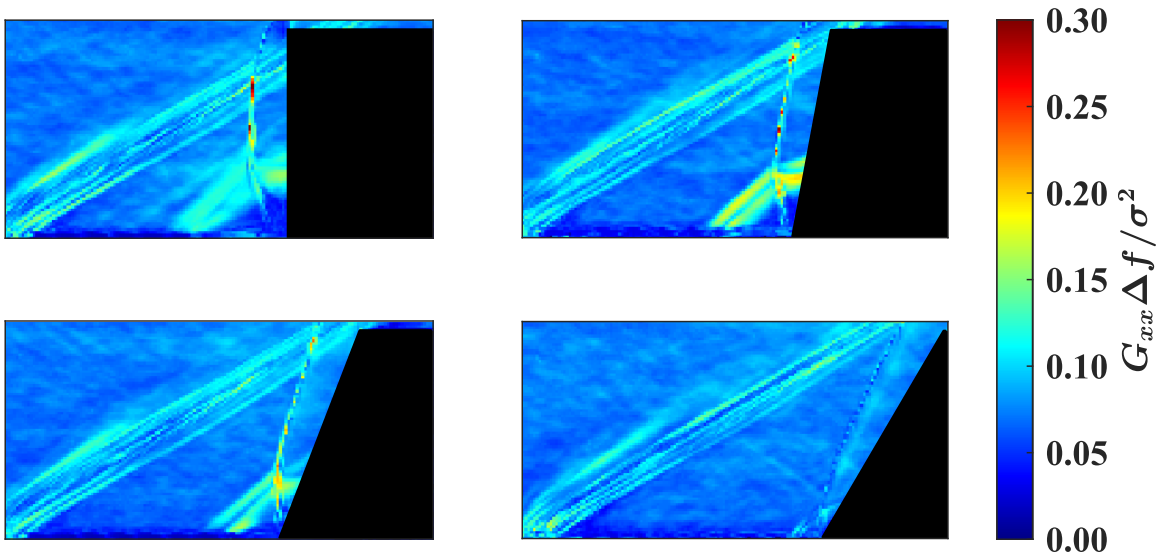

(a) Average PSD images for a frequency band of $1.5 - 3.5$ kHz.

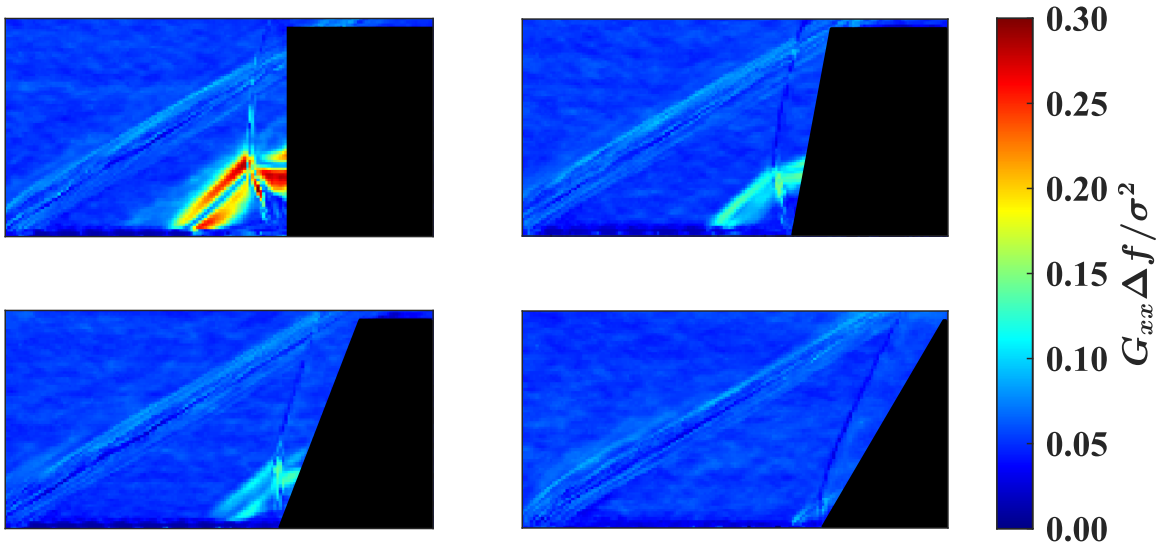

(b) Average PSD images for a frequency band of $4.0 - 6.0$ kHz.

Figure 4.10: Average PSD images for a 2 kHz band centered around the frequency ranges of interest. From left-to-right: $\Lambda = 0°$, $\Lambda = 10°$, $\Lambda = 20°$, $\Lambda = 30°$. NOTE: All images in this figure share the same spatial resolution.

spectra present between 1.5-3.5 kHz range during a linear array focused-laser differential interferometry (LA-FLDI) investigation of the boundary layer in the UTSI Mach 2 facility. This indicates unsteadiness is indeed present at the leading edge of the flat plate due to freestream noise.

4.3.3 Strouhal Number for Separation Shock Position Values

The Strouhal number for the intermittent shock provides further insight into the behavior of the flow at increasing sweep angles. Dolling and Bogdonoff [22, 19] and Gonsalez and Dolling [30] found that the Strouhal number in turbulent cases tends to collapse to a range of $St \simeq 0.01 - 0.03$. As shown in Fig. 4.11 and Table 4.2, the Strouhal number for the unswept fin is $\sim$0.049 which falls within the expected range, $St \simeq 0.01 - 0.1$, for unsteadiness within SBLIs. Previous studies observed that the Strouhal number increases proportionally with the sweep angle of a blunt-fin [9, 30]; however, the results from this experiment do not intially follow the same trend. Clemens and Narayanaswamy [9] discussed the possibility that the increase in Strouhal number with sweep angle could be due to the weakening of the potential feedback mechanism within the separation region. The weaker interaction leads to smaller separation scales, increasing the characteristic frequencies associated with the separation region. Thus producing an increase in the intermittent Strouhal number. The higher Strouhal number for the unswept case may be due to the resonant transitional behavior in the separation region. At $\Lambda = 10^{\circ}$, the peak Strouhal number decreases to $\sim$0.016. At $\Lambda = 20^{\circ}$, the peak Strouhal number increases to $\sim$0.029. This value agrees well with the previous work of Gonsalez and Dolling [30], who observed a range from $St \simeq 0.020 - 0.030$ for various diameter 20° swept fins. The 30° case does not exhibit any peak Strouhal numbers so a value of $\sim$0.020 was chosen based on the (albeit small) local maxima in the $0.015 - 0.030$ range. As previously mentioned, the spectral content does not indicate any strong unsteadiness within the interaction at this sweep angle.

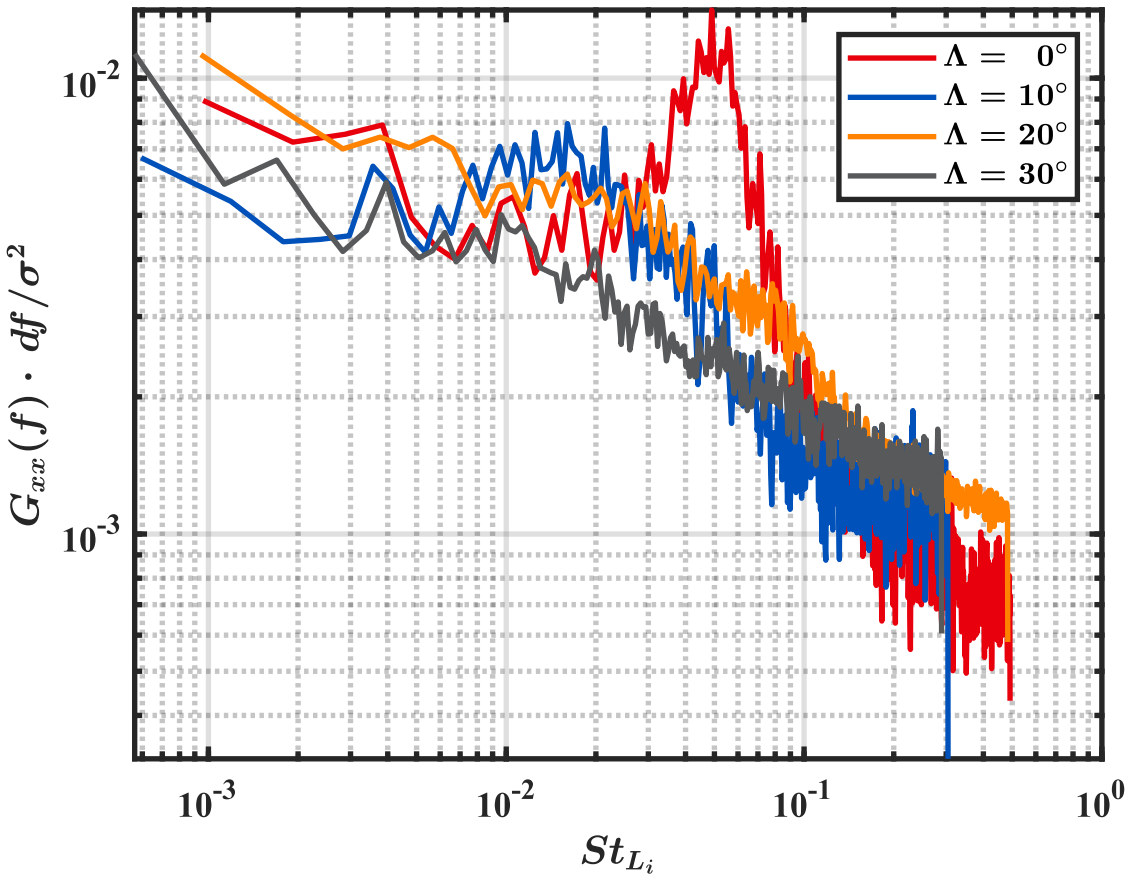

Figure 4.11: St_{L_i} distribution as a function of sweep angle. Note: The beginning and end of the spectral content between each sweep angle varies due to different L_i values. Figure taken from Shoppell et al. [70]

Table 4.2: The peak Strouhal numbers for all sweep cases. NOTE: St_d was included to allow direct comparison to the values reported by Lash et al. [47].

Sweep Angle	$\Lambda = 0°$	$\Lambda = 10°$	$\Lambda = 20°$	$\Lambda = 30°$
f_{max} [kHz]	5.0	2.6	3.0	3.4
L_i [mm]	4.5	2.8	4.4	2.6
U_e $[m/s]$	453	453	453	453
St_{L_i}	0.049	0.016	0.029	0.020
St_d	0.035	0.019	0.021	0.024

Chapter 5

Conclusions and Future Work

5.1 Conclusions

An experimental investigation was conducted to further characterize the fundamental mechanisms that drive the low-frequency unsteadiness in cylinder- and blunt-fin-generated shockwave-boundary layer interactions (SBLI), specifically shockwave-boundary layer interactions in which the incoming boundary layer is undergoing a laminar-to-turbulent transition (XSBLI). The strength of the interaction was varied by introducing sweep angles of $\Lambda = 10°$, $20°$, $30°$ to the blunt-fin in addition to a baseline unswept ($\Lambda = 0°$) case. Due to the streamwise modulation and modification of the narrowband freestream noise reported in the University of Tennessee Space Institute Mach 2 wind tunnel, the effect of the downstream mechanism on the SBLI as a whole can be investigated.

For direct comparison to previously conducted XSBLI research at UTSI [45, 48, 47, 14, 11, 10], the flat plate was installed at angle of attack of $\alpha = -5.5°$ to produce a boundary layer edge Mach number of $M_e \approx 1.78$. The test campaign was conducted at a unit Reynolds number of $31.2 \times 10^6\,\mathrm{m}^{-1}$ A z-type schlieren setup, with a Photron FASTCAM SA-Z, was used to provide a qualitative understanding of the flowfield. Quantitative results such as separation shock foot locations, λ_1, were extracted from the qualitative images using image processing techniques developed within MATLAB. The separation shock foot locations were used to calculate the probability density function (PDF), the streamwise evolution of the zero-crossing frequency, f_c, the streamwise evolution of intermittency, γ_{λ_1}, the power spectral

density (PSD), and the Strouhal number, St_{L_i}. In addition, pressure probes were installed at two streamwise locations to determine if the freestream narrowband noise manifests into the boundary layer. The PSD was calculated for each sensor and the coherence was calculated to determine a direct comparison of spectral content between the two pressure transducers.

The freestream narrowband frequency was measured in the upstream pressure sensor and in the image-based PSD of the leading-edge shockwave. This indicates that the narrowband noise exists throughout the laminar region of the boundary layer, and suggests a potential coupling of the incoming frequency content to the downstream mechanism of the interaction which is extremely sensitive to the incoming boundary layer state when generated by an unswept fin. The unswept case saw excellent agreement to previously reported results. The narrowband content reported at $x/d = 6$ in previous research [45, 48, 47, 14, 11, 10] was detected in the spectral content of the unswept case. The PDF indicated that the unswept interaction covered a larger range of upstream locations, albeit at much lower probabilities than the downstream locations. The Strouhal number of the intermittent region was found to be $St_{L_i} = 0.049$ which was higher than turbulent cases measured by Gonsalez and Dolling [30]; however, when swapping the intermittent length, L_i, with the diameter, d, in the Strouhal number a value of $St_d = 0.035$ was calculated. This aligns extremely well with the diameter-based Strouhal number reported by Lash et al. [47] for an unswept blunt-fin at an $x/d = 6$.

The $\Lambda = 10^\circ$ swept blunt-fin did not exhibit the same narrowband content reported for the unswept case. The spectral content relaxed to a broadband distribution centered around approximately 2.6 kHz and resembled the spectra reported in much of the past XSBLI and STBLI literature [22, 78, 30, 63, 62]. This suggests that the resonant behavior observed in the unswept case was driven by the strength of the underlying mechanisms in the separation region. A peak Strouhal number of $St_{L_i} = 0.016$ was calculated for this condition which showed excellent agreement with the Strouhal numbers reported by Gonsalez and Dolling [30] for swept blunt-fins. The PDF indicated that although the scale of the interaction decreased, the interaction was still highly unsteady and skewed upstream.

The $\Lambda = 20^\circ$ swept blunt-fin exhibited similar broadband spectral content to the 10° case. The spectral content indicated more relaxation of the broadband content occurred with an

increase in sweep angle as the relative power was lower than the 10° case. The broadband content was centered around $f = 3.0$ kHz which correlates to a peak Strouhal number of $St_{L_i} = 0.029$. This condition which showed a nearly identical agreement to the Strouhal numbers reported by Gonsalez and Dolling [30] for a $\Lambda = 20°$ swept blunt-fin. The PDF indicated the scale of the interaction decreased again, but the interaction occurred over a higher range of separation shock foot locations than the 10° case.

The final configuration, the $\Lambda = 30°$ swept blunt-fin exhibited little unsteadiness in the spectral content as the content followed a linear-trend on the logarithmic scale. The separation length scale was comparatively small compared to the other sweep angles and the PDF showed little distribution of the separation shock foot upstream of the mean location. The (extremely small) local maxima in the low-frequency range occurred around $f = 3.4$ kHz which corresponds to a peak Strouhal number of $St_{L_i} = 0.020$. This once again showed great agreement to the Strouhal numbers reported by Gonsalez and Dolling [30] for a $\Lambda = 30°$ swept blunt-fin.

5.2 Future Work

The work reported in this paper opens multiple pathways for future XSBLI research. Interactions on the centerline scale with the boundary layer thickness, δ, and the cylinder diameter, d; however, this needs to be more well-defined for swept interactions. Correlating the unsteadiness in the interaction to incoming boundary layer content at varied sweep angles provides ample opportunities for future research. Such a correlation would be beneficial as an empirical limit for protuberance sweep angles in the design of future aircraft geometries.

In addition, this research provides a future starting point for investigating the relationship between the upstream and downstream unsteadiness mechanisms through freestream narrowband noise generation. Research should be conducted in which the edge conditions of this work are matched in a different facility and perturbed with a 3 kHz frequency in the freestream. If the spectral content of such interactions agreed well with the work completed in the UTSI Mach 2 facility, it would imply a strong correlation between the spectra and the edge Mach number. Subsequently, if such research proved fruitful, XSBLIs could

be perturbed with different coherent tones of narrowband freestream noise to investigate whether there is a dependence between XSBLI resonant tones and freestream acoustic tones.

Bibliography

[1] Anderson, J. D. (2017). *Fundamentals of Aerodynamics*. McGraw-Hill series in aeronautical and aerospace engineering. McGraw Hill Education, New York, NY, sixth edition edition. 30

[2] Anderson, J. D. (2021). *Modern Compressible Flow: with Historical Perspective*. McGraw-Hill series in aeronautical and aerospace engineering. McGraw-Hill Education, Boston, fourth edition edition. 30

[3] Babinsky, H. and Harvey, J. K. (2014). *Shock Wave-Boundary-Layer Interactions*. Cambridge aerospace series. Cambridge university press, Cambridge (GB). 1

[4] Beresh, S. J., Clemens, N. T., and Dolling, D. S. (2002). Relationship Between Upstream Turbulent Boundary-Layer Velocity Fluctuations and Separation Shock Unsteadiness. *AIAA Journal*, 40(12):2412–2422. 14, 16, 18

[5] Bradley, D. and Roth, G. (2007). Adaptive Thresholding using the Integral Image. *Journal of Graphics Tools*, 12(2):13–21. 36

[6] Brown, G. L. and Roshko, A. (1974). On density effects and large structure in turbulent mixing layers. *Journal of Fluid Mechanics*, 64(4):775–816. 15

[7] Brusniak, L. and Dolling, D. S. (1994). Physics of unsteady blunt-fin-induced shock wave/turbulent boundary layer interactions. *Journal of Fluid Mechanics*, 273:375–409. 5

[8] Clemens, N. and Narayanaswamy, V. (2009). Shock/Turbulent Boundary Layer Interactions: Review of Recent Work on Sources of Unsteadiness (Invited). In *39th AIAA Fluid Dynamics Conference*, San Antonio, Texas. American Institute of Aeronautics and Astronautics. 15

[9] Clemens, N. T. and Narayanaswamy, V. (2014). Low-Frequency Unsteadiness of Shock Wave/Turbulent Boundary Layer Interactions. *Annual Review of Fluid Mechanics*, 46(1):469–492. 2, 15, 18, 20, 59

[10] Combs, C. S., Kreth, P. A., Schmisseur, J. D., and Lash, E. L. (2018a). Image-Based Analysis of Shock-Wave/Boundary-Layer Interaction Unsteadiness. *AIAA Journal*, 56(3):1288–1293. 3, 21, 23, 55, 62, 63

[11] Combs, C. S., Lash, E. L., Kreth, P. A., and Schmisseur, J. D. (2018b). Investigating Unsteady Dynamics of Cylinder-Induced Shock-Wave/Transitional Boundary-Layer Interactions. *AIAA Journal*, 56(4):1588–1599. 3, 21, 23, 49, 55, 62, 63

[12] Combs, C. S., Lash, E. L., and Schmisseur, J. D. (2016). Investigation of a Cylinder-Induced Transitional Shock Wave-Boundary Layer Interaction using Laser Diagnostics. In *32nd AIAA Aerodynamic Measurement Technology and Ground Testing Conference*, Washington, D.C. American Institute of Aeronautics and Astronautics. 3

[13] Combs, C. S., Lindörfer, S. A., Kreth, P. A., and Schmisseur, J. D. (2018c). The Role of Boundary-Layer Thickness on Cylinder-Generated Shock-Wave/Turbulent Boundary-Layer Interactions, Part II: Experiments. In *2018 AIAA Aerospace Sciences Meeting*. 3, 21, 23

[14] Combs, C. S., Schmisseur, J. D., Bathel, B. F., and Jones, S. B. (2019a). Analysis of Shock-Wave/Boundary-Layer Interaction Experiments at Mach 1.8 and Mach 4.2. In *AIAA SciTech Forum*. 3, 21, 23, 30, 40, 55, 62, 63

[15] Combs, C. S., Schmisseur, J. D., Bathel, B. F., and Jones, S. B. (2019b). Unsteady Analysis of Shock-Wave/Boundary-Layer Interaction Experiments at Mach 4.2. *AIAA Journal*, 57(11):4715–4724. 3, 21, 23, 55

[16] Cottier, S., Combs, C. S., and Vanstone, L. (2019). Spectral Proper Orthogonal Decomposition Analysis of Shock-Wave/Boundary-Layer Interactions. In *AIAA Aviation 2019 Forum*, Dallas, Texas. American Institute of Aeronautics and Astronautics. 57

[17] Crocco, L. (1937). Eine neue Stromfunktion für die Erforschung der Bewegung der Gase mit Rotation. *ZAMM - Zeitschrift für Angewandte Mathematik und Mechanik*, 17(1):1–7. 24

[18] Davenport, K. and Gragston, M. (2022). Simultaneous Turbulent Boundary Layer Velocity Profile and Scalar Turbulence Spectra with Linear Array-FLDI. In *AIAA SciTech Forum*, San Diego, CA & Virtual. American Institute of Aeronautics and Astronautics. 21, 57

[19] Dolling, D. and Bogdonoff, S. (1981a). An Experimental Investigation of the Unsteady Behavior of Blunt Fin-Induced Shock Wave Turbulent Boundary Layer Interactions. In *14th Fluid and Plasma Dynamics Conference*, Palo Alto,CA,U.S.A. American Institute of Aeronautics and Astronautics. 59

[20] Dolling, D. S. (2001). Fifty Years of Shock-Wave/Boundary-Layer Interaction Research: What's Next? *AIAA Journal*, 39(8):1517–1531. 1

[21] Dolling, D. S. and Bogdonoff, S. M. (1981b). Scaling of Interactions of Cylinders with Supersonic Turbulent Boundary Layers. *AIAA Journal*, 19(5):655–657. 5, 6, 25

[22] Dolling, D. S. and Bogdonoff, S. M. (1982). Blunt fin-induced shock wave/turbulent boundary-layer interaction. *AIAA Journal*, 20(12):1674–1680. 59, 63

[23] Dolling, D. S. and Or, C. T. (1985). Unsteadiness of the Shock Wave Structure in Attached and Separated Compression Ramp Flows. *Experiments in Fluids*, 3(1):24–32. 55

[24] Dupont, P., Piponniau, S., and Dussauge, J. P. (2019). Compressible mixing layer in shock-induced separation. *Journal of Fluid Mechanics*, 863:620–643. 15, 18

[25] Erengil, M. E. and Dolling, D. S. (1991). Unsteady Wave Structure near Separation in a Mach 5 Compression Ramp Interaction. *AIAA Journal*, 29(5):728–735. 55

[26] Erengil, M. E. and Dolling, D. S. (1993). Effects of Sweepback on Unsteady Separation in Mach 5 Compression Ramp Interactions. *AIAA Journal*, 31(2):302–311. 14

[27] Ganapathisubramani, B., Clemens, N. T., and Dolling, D. S. (2006). Large-scale motions in a supersonic turbulent boundary layer. *Journal of Fluid Mechanics*, 556:271. 14, 20

[28] Ganapathisubramani, B., Clemens, N. T., and Dolling, D. S. (2007). Effects of Upstream Boundary Layer on the Unsteadiness of Shock-Induced Separation. *Journal of Fluid Mechanics*, 585:369–394. 20

[29] Ganapathisubramani, B., Clemens, N. T., and Dolling, D. S. (2009). Low-frequency dynamics of shock-induced separation in a compression ramp interaction. *Journal of Fluid Mechanics*, 636:397–425. 20

[30] Gonsalez, J. and Dolling, D. (1993). Correlation of Interaction Sweepback Effects on Unsteady Shock-Induced Turbulent Separation. In *31st Aerospace Sciences Meeting*. American Institute of Aeronautics and Astronautics. 16, 18, 57, 59, 63, 64

[31] Hirschel, E. H. (2015). *Basics of Aerothermodynamics*. Springer International Publishing : Imprint: Springer, Cham, 2nd ed. 2015 edition. 45

[32] Hoffman, E. N. A., Rodriguez, J. M., Cottier, S. M., Combs, C. S., Bathel, B. F., Weisberger, J. M., Jones, S. B., Schmisseur, J. D., and Kreth, P. A. (2022). Modal Analysis of Cylinder-Induced Transitional Shock-Wave/Boundary-Layer Interaction Unsteadiness. *AIAA Journal*, 60(5):2730–2748. 57

[33] Holden, M. (1986). A Review of Aerothermal Problems Associated with Hypersonic Flight. In *24th Aerospace Sciences Meeting*, Reno,NV,U.S.A. American Institute of Aeronautics and Astronautics. 1

[34] Hooke, R. (1667). *Micrographia, Or, Some Physiological Descriptions of Minute Bodies Made by Magnifying Glasses. With Observations and Inquiries Thereupon*. History of microscopy series. Science Heritage. 30

[35] Hou, Y., Clemens, N. J., and Dolling, D. (2003). Wide-Field PIV Study of Shock-Induced Turbulent Boundary Layer Separation. In *41st Aerospace Sciences Meeting and Exhibit*, Reno, Nevada. American Institute of Aeronautics and Astronautics. 14, 18

[36] Humble, R., Elsinga, G., Scarano, F., and van Oudheusden, B. (2007a). Investigation of the Instantaneous 3D Flow Organization of a SWTBLI Using Tomographic PIV. In

37th AIAA Fluid Dynamics Conference and Exhibit, Miami, Florida. American Institute of Aeronautics and Astronautics. 14

[37] Humble, R. A., Elsinga, G. E., Scarano, F., and van Oudheusden, B. W. (2007b). Experimental Investigation of the Three-Dimensional Structure of a Shock Wave/Turbulent Boundary Layer Interaction. In Jacobs, P., editor, *16 AFMC: proceedings of the sixteenth Australasian Fluid Mechanics Conference, 3-7 December, 2007, Gold Coast, Australia*, St. Lucia, Qld. School of Engineering, University of Queensland. OCLC: 1369577972. 14

[38] Humble, R. A., Elsinga, G. E., Scarano, F., and van Oudheusden, B. W. (2009). Three-dimensional instantaneous structure of a shock wave/turbulent boundary layer interaction. *Journal of Fluid Mechanics*, 622:33–62. 14

[39] Humble, R. A., Scarano, F., and van Oudheusden, B. W. (2007c). Particle image velocimetry measurements of a shock wave/turbulent boundary layer interaction. *Experiments in Fluids*, 43(2-3):173–183. 14

[40] John, J. E. A. and Keith, T. G. (2006). *Gas Dynamics*. Pearson Prentice Hall, Upper Saddle River, N.J, 3rd ed edition. OCLC: ocm62133814. 30

[41] Korkegi, R. H. (1973). A Simple Correlation for Incipient-Turbulent Boundary-Layer Separation due to a Skewed Shock Wave. *AIAA Journal*, 11(11):1578–1579. 16, 45

[42] Kulite Semiconductor Products, Inc (2023a). KSC-2. Datasheet, Kulite Semiconductor Products, Inc, Leonia, NJ. 34

[43] Kulite Semiconductor Products, Inc (2023b). XCQ-SL-062 Series. Datasheet, Kulite Semiconductor Products, Inc, Leonia, NJ. 34

[44] Kulite Semiconductor Products, Inc (2023c). XCS-062 Series. Datasheet, Kulite Semiconductor Products, Inc, Leonia, NJ. 34

[45] Lash, E. L., Combs, C. S., Kreth, P. A., and Schmisseur, J. D. (2017a). Experimental Investigation of a Cylinder-Induced Transitional Shock Wave-Boundary Layer Interaction. In *55th AIAA Aerospace Sciences Meeting*. 3, 21, 23, 55, 62, 63

[46] Lash, E. L., Combs, C. S., Kreth, P. A., and Schmisseur, J. D. (2017b). Study of the Dynamics of Transitional Shock Wave-Boundary Layer Interactions using Optical Diagnostics. In *47th AIAA Fluid Dynamics Conference*. 3, 23, 55

[47] Lash, E. L., Gragston, M., Kreth, P. A., McDaniel, Z., Coder, J. G., and Schmisseur, J. D. (2021). Upstream Influence in Shock Wave/Transitional Boundary Layer Interactions at Mach 1.8. *AIAA Journal*, 59(12):4842–4857. 3, 5, 8, 10, 16, 20, 21, 23, 25, 40, 45, 55, 61, 62, 63

[48] Lash, E. L., Gragston, M., McDaniel, Z., Kreth, P. A., and Schmisseur, J. D. (2020). Exploration of Upstream Influence and the Role of Shock Generator Geometry in Shock Wave/Transitional Boundary Layer Interactions at Mach 1.8 Edge Conditions. In *AIAA AVIATION 2020 Forum*. 3, 21, 23, 55, 62, 63

[49] Lindörfer, S. A. (2017). A Numerical Study of the Limiting Cases of Cylinder-Induced Shock Wave/Boundary Layer Interactions. Master's thesis, University of Tennessee. 2, 5

[50] Lindörfer, S. A., Combs, C. S., Bond, R. B., and Schmisseur, J. D. (2018). The Role of Boundary-Layer Thickness on Cylinder-Generated Shock-Wave/Turbulent Boundary-Layer Interactions, Part I: Computations. In *2018 AIAA Aerospace Sciences Meeting*. 20

[51] Lindörfer, S. A., Combs, C. S., Kreth, P. A., Bond, R. B., and Schmisseur, J. D. (2017). Limiting Cases for Cylinder-Induced Shock Wave/Boundary Layer Interactions. In *47th AIAA Fluid Dynamics Conference*. 20

[52] Lindörfer, S. A., Combs, C. S., Kreth, P. A., Bond, R. B., and Schmisseur, J. D. (2020). Scaling of cylinder-generated shock-wave/turbulent boundary-layer interactions. *Shock Waves*, 30(4):395–407. 6, 7, 25

[53] Mack, L. (1974). On the application of linear stability theory to the problem of supersonic boundary-layer transition. In *12th Aerospace Sciences Meeting*, Washington,DC,U.S.A. American Institute of Aeronautics and Astronautics. 14

[54] Mack, L. M. (1975). Linear Stability Theory and the Problem of Supersonic Boundary-Layer Transition. *AIAA Journal*, 13(3):278–289. 14

[55] Morkovin, M. V. (1962). Effects of Compressibility on Turbulent Flows. In *Favre, A. (Ed.), Mécanique de la Turbulence*, Paris. CNRS. 11, 12

[56] Morkovin, M. V. (1969). On the Many Faces of Transition. In *Wells, C.S. (eds) Viscous Drag Reduction*, pages 1–31, Boston, MA. Springer. 11, 12

[57] Morkovin, M. V. (1988). Recent insights into instability and transition to turbulence in open-flow systems. Contractor Report NASA-CR-181693, National Aeronautics and Space Administration. 11, 12

[58] Navier, C. (1839). *Resume Des Lecons Donnees A L'Ecole Des Ponts Et Chaussees Sur L'Application De La Mecanique A L'Etablissement Des Constructions Et Des Machines. Seconde Partie, Contenant Les Lecons Sur Le Mouvement Et La Resistance Des Fluides, Et Sur La Conduite Et La Distribution Des Eaux.* Societe Belge de Librairie. 20

[59] Otsu, N. (1979). A Threshold Selection Method from Gray-Level Histograms. *IEEE Transactions on Systems, Man, and Cybernetics*, 9(1):62–66. 36

[60] Piponniau, S., Dussauge, J. P., Debiève, J. F., and Dupont, P. (2009). A simple model for low-frequency unsteadiness in shock-induced separation. *Journal of Fluid Mechanics*, 629:87–108. 15, 20

[61] Pirozzoli, S. and Grasso, F. (2006). Direct numerical simulation of impinging shock wave/turbulent boundary layer interaction at M=2.25. *Physics of Fluids*, 18(6):065113. 15, 16, 20, 24, 57

[62] Plotkin, K. J. (1975). Shock Wave Oscillation Driven by Turbulent Boundary-Layer Fluctuations. *AIAA Journal*, 13(8):1036–1040. 63

[63] Poggie, J. and Smits, A. J. (2001). Shock Unsteadiness in a Reattaching Shear Layer. *Journal of Fluid Mechanics*, 429:155–185. 63

[64] Price, T. (2022). *Experimental Investigation of Supersonic Jets Using Optical Diagnostics*. PhD Dissertation, University of Tennessee. 30

[65] Priebe, S. and Martín, M. P. (2012). Low-frequency unsteadiness in shock wave–turbulent boundary layer interaction. *Journal of Fluid Mechanics*, 699:1–49. 16, 18

[66] Reynolds, O. (1895). IV. On the dynamical theory of incompressible viscous fluids and the determination of the criterion. *Philosophical Transactions of the Royal Society of London. (A.)*, 186:123–164. 20

[67] Saric, W. S., Reed, H. L., and Kerschen, E. J. (2002). Boundary-Layer Receptivity to Freestream Disturbances. *Annual Review of Fluid Mechanics*, 34(1):291–319. 11

[68] Settles, G. and Dolling, D. (1990). Swept Shock/Boundary-Layer Interactions - Tutorial and update. In *28th Aerospace Sciences Meeting*. American Institute of Aeronautics and Astronautics. 5

[69] Settles, G. S. (2001). *Schlieren and Shadowgraph Techniques: Visualizing Phenomena in Transparent Media*. Experimental fluid mechanics. Springer, Berlin Heidelberg, softcover reprint of the hardcover 1st edition 2001 edition. 30, 31

[70] Shoppell, Z. M., Langley, K. R., and Schmisseur, J. D. (2023). Experimental Investigation of the Role of Shock Strength in Transitional Shockwave-Boundary Layer Interactions. In *AIAA SCITECH 2023 Forum*, National Harbor, MD & Online. American Institute of Aeronautics and Astronautics. 8, 9, 27, 29, 32, 47, 48, 52, 54, 56, 60

[71] Souverein, L., Dupont, P., Debiève, J.-F., Dussauge, J.-P., van Oudheusden, B., and Scarano, F. (2009). Effect of Interaction Strength on the Unsteady Behavior of Shock Wave Boundary Layer Interactions. In *39th AIAA Fluid Dynamics Conference*, San Antonio, Texas. American Institute of Aeronautics and Astronautics. 15

[72] Souverein, L. J., Dupont, P., Debiève, J.-F., Dussauge, J.-P., van Oudheusden, B. W., and Scarano, F. (2010). Effect of Interaction Strength on Unsteadiness in Shock-Wave-Induced Separations. *AIAA Journal*, 48(7):1480–1493. 15

[73] Stoica, P. and Moses, R. L. (2005). *Spectral Analysis of Signals*. Pearson/Prentice Hall, Upper Saddle River, N.J. 39

[74] Stokes, G. G. (1845). On the Theories of the Internal Friction of Fluids in Motion, and of the Equilibrium and Motion of Elastic Solids. *Transactions of the Cambridge Philosophical Society*, 8:287–305. 20

[75] Tester, B. W., Coder, J. G., Combs, C. S., and Schmisseur, J. D. (2018). Hybrid RANS/LES Simulation of Transitional Shockwave/Boundary-Layer Interaction. In *2018 Fluid Dynamics Conference*, Atlanta, Georgia. American Institute of Aeronautics and Astronautics. 16, 17, 19, 20

[76] The MathWorks, Inc. (2023a). Binarize 2-D grayscale image or 3-D volume by thresholding - MATLAB imbinarize. 36

[77] The MathWorks, Inc. (2023b). MATLAB R2023a. 36, 38

[78] Threadgill, J. A. S. and Bruce, P. J. K. (2020). Unsteady Flow Features Across Different Shock/Boundary-Layer Interaction Configurations. *AIAA Journal*, 58(7):3063–3075. 63

[79] Threadgill, J. A. S., Little, J. C., and Wernz, S. H. (2021). Transitional Shock Boundary Layer Interactions on a Compression Ramp at Mach 4. *AIAA Journal*, 59(12):4824–4841. 5, 8

[80] Toepler, A. (1864). *Beobachtungen Nach Einer Neuen Optischen Methode - Ein Beitrag zur Experimentalphysik*. M. Cohen & Son, Bonn, Germany. 30

[81] Toepler, A. (1906). *Beobachtungen Nach Der Schlierenmethode*. Number 158 in Ostwalds Klassiker Der Exakten Wissenschaften. W. Engelmann, Leipzig. 30

[82] Touber, E. and Sandham, N. D. (2011). Low-Order Stochastic Modelling of Low-Frequency Motions in Reflected Shock-Wave/Boundary-Layer Interactions. *Journal of Fluid Mechanics*, 671:417–465. 15, 18, 20, 24

[83] Truitt, R. W. (1965). Hypersonic turbulent boundary-layer interference heat transfer in vicinity of protuberances. *AIAA Journal*, 3(9):1754–1755. 5

[84] Watts, J. D. (1968). Flight experience with shock impingement and interference heating on the X-15-2 research airplane. *NASA TM X-1669*. 1

[85] Welch, P. (1967). The use of fast Fourier transform for the estimation of power spectra: A method based on time averaging over short, modified periodograms. *IEEE Transactions on Audio and Electroacoustics*, 15(2):70–73. 39

[86] White, E. B., Saric, W. S., and Radeztsky, R. H. (2000). Leading-Edge Acoustic Receptivity Measurements Using a Pulsed-Sound Technique. In *Laminar-Turbulent Transition: IUTAM Symposium, Sedona/AZ September 13–17, 1999*, Berlin Heidelberg. Springer. 24

[87] White, F. M. (2006). *Viscous Fluid Flow*. McGraw-Hill series in mechanical engineering. McGraw-Hill Higher Education, New York, NY, 3rd edition. 7, 11, 16, 45

[88] Zhong, X. (1998). High-Order Finite-Difference Schemes for Numerical Simulation of Hypersonic Boundary-Layer Transition. *Journal of Computational Physics*, 144(2):662–709. 11, 24

[89] Zhong, X. and Wang, X. (2012). Direct Numerical Simulation on the Receptivity, Instability, and Transition of Hypersonic Boundary Layers. *Annual Review of Fluid Mechanics*, 44(1):527–561. 11, 13, 24

Appendices

A Use of Figures from Published Works

NASA Media Usage Guidelines

NASA outlines the following guidelines for use of digital media:

> News outlets, schools, and text-book authors may use NASA content without needing explicit permission, subject to compliance with these guidelines. NASA content used in a factual manner that does not imply endorsement may be used without needing explicit permission. NASA should be acknowledged as the source of the material. NASA occasionally uses copyright-protected material of third parties with permission on its website. Those images will be marked identified as copyright protected with the name of the copyright holder. NASA's use does not convey any rights to others to use the same material. Those wishing to use copyright protected material of third parties must contact the copyright holder directly.

For further information on these policies visit:
https://www.nasa.gov/multimedia/guidelines/index.html

STM and PSP Guidelines for Quotation and Other Academic Uses of Excerpts from Journal Articles

The International Association of Scientific, Technical & Medical Publishers (STM) and the Professional Scholarly & Publishing division of the Association of American Publishers (PSP) outline the following guidelines for the use of material in limited amounts:

> Publishers accept that scholarly articles often require the direct reproduction of illustrative material (such as figures, tables, structures) for the purposes of discussion or comparison with other data, and that the electronic version of an article needs to contain the same illustrative material in order to maintain the

authenticity of the record in both print and digital form. Publishers accept that the use of short quotations is normal in scholarship, generally intended to place the new work in scholarly context or to comment on the quoted work or its impact, and that there is minimal potential in such practices of negatively impacting the demand for the original work.

With respect to the use of small portions of journal articles by academics and scholars, or the institutions in which they conduct their research or educational work, that scholars (or their institutions with respect to course-packs) may (without obtaining explicit permission from publishers):

- Use a maximum of two figures (including tables) from a journal article or five figures per journal volume (unless a separate copyright holder is identified in such figure, in which event permission should be sought from that holder);
- Use single text extracts of less than 100 words or series of text extracts totaling less than 300 words for quotation; and
- Use such excerpts in all media and in future editions.

The following conditions apply:

- The purpose of the use is scholarly comment or non-commercial research or educational use;
- Certain complex illustrations such as anatomical drawings; cartoons; maps; poetry; works of art; or photographs, will still require normal permissions requests of publishers (or other copyright holder) as the journal article author(s) is unlikely to own the copyright in these;
- Full credit should be given to the author(s) and publisher(s) of the material(s) used, consistent with normal scholarly practice; and
- The quotation or excerpt must never be modified.

Note that some scholarly societies that own journals published on their behalf by another publisher may have more restrictive policies on permissions than those

of the publisher, and the publisher, journal administrator or the journal's web site may need to be consulted with respect to such policies (check the copyright notice to see if there is a copyright owner other than the publisher).

These Guidelines are intended to help reduce legal uncertainty and improve and simplify administrative procedures with respect to the use of short excerpts of scholarly and professional information from journal articles. The participating publishers believe that by establishing clear guidance, research and scholarship as a whole is improved and scientific communication and education are made more effective and efficient.

Publisher signatories:

AIP Publishing

American Chemical Society

BMJ Publishing Group Ltd

Elsevier

Institute of Physics

International Union of Crystallography

John Wiley & Sons (including Blackwell)

Oxford University Press Journals

Portland Press Limited

Royal Society of Chemistry

SAGE Publications

Springer Science+Business Media

Taylor & Francis

For further information on these policies visit:

https://www.stm-assoc.org

B Selected Scripts

B.1 Shock Tracker

```
%%%%%%%%%%%%%%%%%%%%%%%%%%%%%%%%%%%%%%%%%%%%%%%%%%%%%%%%%%%%%%%%%%%%%%%
%                                                                       %
%                      Zane M. Shoppell                                 %
%                           HORIZON                                     %
%                     Updated: 4/25/2023                                %
%                                                                       %
%%%%%%%%%%%%%%%%%%%%%%%%%%%%%%%%%%%%%%%%%%%%%%%%%%%%%%%%%%%%%%%%%%%%%%%


%% Select data from file
foldername = sprintf('C:/Users/zshoppel/Documents/SciTECH23...
/20220210_shoppell_flatplate_fin0_2/');
filetype = '*.tif'; % File type extension
a = dir(append(foldername,filetype));
% Change this to select range of images
% number = length(a);
angle = 5.5;
xx = zeros(1,number);

%% Begin Frame-by-Frame "Streaming"
for n = 1:number
file = [foldername,a(n).name];
picture = imread(file);
picture = im2gray(picture); % ensures image is grayscale
picture = flip(picture,2); % flips image to match flow
   convention
```

```
picture = imrotate(picture,-5.5,'bicubic'); % rotates image to
   align with flat plate
picture = picture(129:207,120:220); % crops image from leading
   edge to shock generator face

%% Threshold to extract shock structure
% convert image to binary with a dark foreground polarity set
% at 5-10%
% (adjust for different data sets) so the dark values shown
% represent the foot shock

BW = imbinarize(picture,'adaptive','ForegroundPolarity',...
'dark','Sensitivity',0.09);
% Remove LE shock artifacts in images
BW(1:60,1:60) = true(1,1);

%% Choose Region of Interest (separation or reattachment shock)

% Separation Shock Interrogation (Adjust values to change
% interogation region)
start = [60,50]; % starting pixels
w = 26; % width
h = 26; % height

% Closure Shock Interrogation (Adjust values to change
% interogation region)
% start = [101-98,58]; % starting pixels
% w = 10; % width
% h = 15; % height
```

```
% Define Region of Interest
% rows to be interrogated, use as y if not working in matrix
% coordinates
r = start(2):1:(start(2)+h);
% columns to be interrogated, use as x if not working in matrix
% coordinates
c = start(1):1:(start(1)+w);

% Find shock location
[~,col]=min(BW(r,c),[],2);
col(col==1) = NaN;
col = (col+start(1)-1);
r = r.';
r(isnan(col)) = NaN;
loc = [r,col]; % Shock location

% Extrapolation
x1 = col(1);
y1 = r(1)
% Equation for slope
m = (r(end) - y1)./(col(end)-x1);
 % Ensures constant extrapolation in the wall-normal direction
 y2 = 77;
xx(n) = (y2-y1)./m + x1;

%% Plot tracker over image (comment to disable plotting
% and decrease run time)
% figure(1);

% newScale = 1;
```

```
% Uncomment this one for binary image
% BW = imresize(BW,newScale,"lanczos3");
% imshow(BW);

% Uncomment this one for schlieren image
% picture = imresize(picture,newScale,"lanczos3");
% imshow(picture);

% Uncomment this for both schlieren and binary images overlaid
   with tracker
% imshowpair(picture,pic,'montage');
% hold on;
% plot([(start(1)+w)*newScale,xx(n)*newScale-2],[(y2+...
% ((start(1)+w)-xx(n)).*m)*newScale-2,y2*newScale],...
% 'r','LineWidth',0.5*newScale);
% hold off;
% axis image
% pause(0.5) % Defines how long each frame will display on
   screen
end

% Indicate done running
beep;
```

Vita

Zane Matthew Shoppell was born in South Bend, Indiana, on August 19th, 1998. He grew up in White Pigeon, Michigan, and graduated from White Pigeon High School in May 2017. Zane spent most of his undergraduate career at the University of Kansas, where he received his B.S. in Aerospace Engineering in May of 2021. Immediately following graduation, he began work towards his M.S. in Aerospace Engineering at the University of Tennessee Space Institute with the HORIZON Research Group. He successfully defended his thesis on April 14th, 2023, and obtained his M.S. in Aerospace Engineering with a Thermal-Fluid Mechanics Concentration in the Spring of 2023. Zane plans to stay at the University of Tennessee Space Institute to pursue his Ph.D. in Aerospace Engineering while continuing his research with the HORIZON Research Group.